

# The dust effects on galaxy scaling relations

Bogdan A. Pastrav<sup>1</sup>★

<sup>1</sup>*Cosmology and Astroparticle Physics Laboratory, Institute of Space Science, Atomistilor 409, 077125, Bucharest-Magurele, Romania*

Accepted 2020 February 12. Received 2019 December 13; in original form 2019 June 27

## ABSTRACT

Accurate galaxy scaling relations are essential for a successful model of galaxy formation and evolution as they provide direct information about the physical mechanisms of galaxy assembly over cosmic time. We present here a detailed analysis of a sample of nearby spiral galaxies taken from the KINGFISH survey. The photometric parameters of the morphological components are obtained from bulge-disk decompositions using GALFIT data analysis algorithm, with surface photometry of the sample done beforehand. Dust opacities are determined using a previously discovered correlation between the central face-on dust opacity of the disk and the stellar mass surface density. The method and the library of numerical results previously obtained are used to correct the measured photometric and structural parameters for projection (inclination), dust and decomposition effects in order to derive their intrinsic values. Galaxy disk scaling relations are then presented, both the measured (observed) and the intrinsic (corrected) ones, in the optical regime, to show the scale of the biases introduced by the aforementioned effects. The slopes of the size-luminosity relations and the dust vs stellar mass are in agreement with values found in other works. We derive mean dust optical depth and dust/stellar mass ratios of the sample, which we find to be consistent with previous studies of nearby spiral galaxies. While our sample is rather small, it is sufficient to quantify the influence of galaxy environment (dust, in this case) when deriving scaling relations.

**Key words:** galaxies: spiral – galaxies: photometry – galaxies: structure – ISM: dust, extinction – galaxies: evolution – galaxies: fundamental parameters

## 1 INTRODUCTION

Galaxy scaling relations - the understanding of their nature and why they exist - are of pivotal importance in a successful theory/model of galaxy formation and evolution. Thus, a valid semi-analytic model or a numerical simulation should be able to predict with great accuracy the characteristics of galaxy scaling relations, such as slope, zero point and scatter, at any wavelength. These relations are also important because they provide direct insights into the physical mechanisms of how galaxies and their main components assemble over cosmic time. Basic scaling relations (e.g. size-luminosity/surface brightness, Tully-Fisher (Tully & Fisher 1977), Faber-Jackson (Faber & Jackson 1976), Kormendy (Kormendy 1977) relation, the Fundamental Plane (Djorkovsky & Davis 1987), star-formation vs stellar mass, etc.) rely on photometric and structural parameters such as disk scalelength, bulge effective radius and Sérsic index, luminosity / surface brightness, absolute magnitudes, circular velocity / velocity dispersion, bulge-to-disk ratio etc.. Most of these parameters suffer from biases introduced by dust and inclination, especially in spiral galaxies, where dust is present in copious quantities in the disk (Tuffs et al. 2002, Popescu et al. 2002, Stickel et al. 2004, Vlahakis et al. 2005, Driver

et al. 2007, Dariush et al. 2011, Rowlands et al. 2012, Bourne et al. 2012, Dale et al. 2012). These effects are stronger at shorter wavelengths and at higher inclinations, as already shown by Tuffs et al. (2004), Möllenhoff et al. (2006), Gadotti et al. (2010), Pastrav et al. (2013a) and Pastrav et al. (2013b). Therefore, one should first remove all these biases when analysing galaxy scaling relations from observational studies.

Previous works to derive intrinsic scaling relations, corrected for the effects of dust and inclination are currently lacking. Among them, Graham & Worley (2008) is noteworthy. They used the radiative transfer model of Popescu et al. (2000) and numerical corrections from Möllenhoff et al. (2006) for the disk brightness and scale-length, to analyse the intrinsic (dust corrected) luminosity-size and (surface-brightness)-size relations for discs and bulges. However, the study of Möllenhoff et al. (2006) was done for pure disks only, at low to intermediate inclinations. Other studies quantifying dust effects on disk photometric parameters are the ones done by Byun et al. (1994), Evans (1994) and Cunow (2001). Gadotti et al. (2010) studied the effects of dust attenuation on both bulge and disk structural parameters, through simulations produced with Monte Carlo radiative transfer technique and bulge-disk decompositions. Grootes et al. (2013) used a correlation between dust opacity and stellar mass surface density that they had identified, together with the radiation transfer model of Popescu et al. (2011) to

★ E-mail: bapastrav@spacescience.ro

derive scaling relations for specific star formation rate, stellar mass and stellar mass surface density. By removing the biases introduced by dust and projection effects, they were able to reduce the scatter in those relations. More recently, [Devour & Bell \(2017\)](#) presented an inclination-independent technique (linear surface brightness) to measure sizes and concentrations of infrared selected samples of disk and flattened elliptical galaxies and showed how structural parameters are biased by projection effects.

In this paper we present the results of a detailed study of a sample of nearby unbarred spiral galaxies from the KINGFISH survey ([Kennicutt et al. 2011](#)), showing dust biases in disk scaling relations of spiral galaxies. For this purpose, we decompose each galaxy into its main components (bulge+disk), deriving intrinsic parameters involved in the scaling relations. We follow the method of [Pastrav et al. \(2013a\)](#) and [Pastrav et al. \(2013b\)](#) and use their numerical corrections for projection (inclination), dust and decomposition effects. The numerical corrections were derived by analysing and fitting simulated images of galaxies produced by means of radiative transfer calculations and the model of [Popescu et al. \(2011\)](#). We also use the empirical relation found by [Grootes et al. \(2013\)](#) to determine the central face-on dust opacity. This is necessary when applying the corrections for dust effects.

The method presented here is suitable for cases when optical data is available. Our study comes to underline the importance of having accurate, dust-free scaling relations in models and studies of galaxy formation and evolution (the size-luminosity type relations, stellar mass vs size), or the interstellar medium (ISM) evolution (relations such as dust mass vs stellar mass, dust-to-stellar ratio as a function of stellar mass or stellar mass surface density). The size of our sample is sufficient for the purpose of this work. This study is an application of the results obtained in [Pastrav et al. \(2013a\)](#) and [Pastrav et al. \(2013b\)](#) and the first which takes all the aforementioned effects to obtain truly intrinsic scaling relations.

The paper is organised as follows. In Sect. 2 we present the galaxy sample used in this study, while in Sect. 3 we present the method used for deriving the integrated fluxes, background subtraction and the overall fitting procedure. In Sect. 3.3 we present the relations used to derive dust opacities and masses and then, in sect. 3.4, our method to correct the derived structural and photometric parameters for inclination, dust and decomposition effects. In Sect. 4 we present the main results, plots with galaxy scaling relations, both observed and intrinsic (dust-free) ones, all the numerical results and comment upon them. In Sect. 5 there is a short discussion concerning some of the results, while in Sect. 6 we summarise the results obtained in this study and draw conclusions. Throughout this paper, where necessary, a Hubble constant of  $H_0 = 67.8$  km/s/Mpc (Planck Collaboration 2016) was used.

## 2 SAMPLE

Our sample consists of 18 nearby spiral galaxies, included in the SINGS (*Spitzer* Infrared Nearby Galaxies Survey; [Kennicutt et al. 2003](#)) survey and the KINGFISH project (Key Insights on Nearby Galaxies: a Far-Infrared Survey with *Herschel*; [Kennicutt et al. 2011](#)). The KINGFISH project is an imaging and spectroscopic survey, consisting of 61 nearby ( $d < 30$  Mpc) galaxies, chosen to cover a wide range of galaxy properties (morphologies, luminosities, SFR, etc.) and local ISM environments characteristic for the nearby universe.

We extracted the optical images from the NASA/IPAC Infrared Science Archive (IRSA) and NASA IPAC Extragalactic Database

(NED). The images were taken with the KPNO (Kitt Peak National Observatory) and CTIO (Cerro Tololo Inter-American Observatory) telescopes (see [Kennicutt et al. \(2003\)](#)). From this sample, we exclude elliptical, irregular or dwarf galaxies, as these are not appropriate for the purpose and methods used in this study. We also exclude barred galaxies. This is done because we want to observe dust-free scaling relations, and, at this point, we cannot properly account for the effects of dust on the photometric and structural parameters of bars. Of course, one could do a 2-component decomposition (disk+bulge) instead of a 3-component one (disk+bulge+bar) for the barred galaxies, but this would bias the results obtained for the bulge component parameters, producing an overestimation of  $B/T$  or bulge Sérsic index, as [Laurikainen et al. \(2006\)](#) have shown (a fraction of the bar surface brightness could be mixed into the bulge one, while another fraction could be embedded in the disk surface brightness).

Therefore, after taking into account these considerations, we are left with a sample of 18 unbarred nearby spiral galaxies, in B band. We have considered for our study the analysis of galaxy images in the optical regime (B band), as dust and inclination effects are stronger at shorter wavelengths ([Pastrav et al. \(2013a\)](#), [Pastrav et al. \(2013b\)](#)), and because our method is tailored for cases where optical data are available.

## 3 METHOD

### 3.1 Fitting procedure

We used GALFIT (version 3.0.2) data analysis algorithm ([Peng et al. 2002](#), [Peng et al. 2010](#)) for the fitting procedure of the galaxy images in our sample. GALFIT uses a non-linear least-squares fitting based on the Levenberg-Marquardt algorithm. Through this, the goodness of the fit is checked by computing the  $\chi^2$  between the the real galaxy image and the model image (created by GALFIT to fit the galaxy image). This is an iterative process, and the free parameters corresponding to each component are adjusted after each iteration to minimize the normalised (reduced) value of  $\chi^2$  ( $\chi^2/N_{DOF}$ , with  $N_{DOF}$  = number of pixels - number of free parameters, the number of degrees of freedom).

To fit the observed images of the unbarred spiral galaxies and perform bulge-disk decomposition we used the exponential (“expdisk”) and the Sérsic (“seraic”) functions available in GALFIT, for the disk and bulge surface brightness profiles, together with the “sky” function (for an estimation of the background in each image). The two functions represent the distribution of an infinitely thin disk, and their mathematical description is given by Eqs. 1 and 2, below:

$$\mu(r) = \mu_0 \exp\left(-\frac{r}{R_{s,d}}\right) \quad (1)$$

$$\mu(r) = \mu_0 \exp\left[-\kappa_n \left(\frac{r}{R_{e,b}}\right)^{1/n}\right] \quad (2)$$

where  $\mu_0$  is the central surface brightness of the infinitely thin disk,  $R_{s,d}$  and  $R_{e,b}$  are the scale-length of the disk and the effective radius of the bulge,  $n$  is the Sérsic index, while  $\kappa_n$  is a variable coupled with  $n$  (see Eq. 3 or [Ciotti & Bertin 1999](#) and [Graham & Driver 2005](#)).

$$\kappa_n = 2n - \frac{1}{3} + \frac{4}{405n} + \frac{46}{25515n^2} + O(n^{-3}) \quad (3)$$

The free parameters of the fits are: the X and Y coordinates of the centre of the galaxy in pixels, the integrated magnitudes of the disk

and bulge components, the scale-length / effective radius (for exponential/Sérsic function), axis-ratios, and bulge Sérsic index (for Sérsic function), the sky background (in the preliminary fit - Step 1) and the sky gradients in X and Y. Although the central coordinates are free parameters, we imposed a constraint on the fitting procedure, ensuring that the bulge and disk components were centred on the same position. The axis-ratio is defined as the ratio between the semi-minor and semi-major axis of the model fit (for each component). The position angle is the angle between the semi-major axis and the Y axis (increasing counter clock-wise).

We did not use a “sigma” image internally created by GALFIT. Instead, we used a complex star-masking routine to eliminate the additional light coming from neighboring galaxies, stars, compact sources, AGN or image artifacts, for each galaxy image, and therefore mask the corresponding bad pixels. These images were introduced as bad pixel masks in each run of GALFIT. To create separate images for the components of each galaxy (disk and bulge), we used the functionalities of GALFIT. The images were needed as a way to determine the value of  $B/D$  and compare it with the corresponding value derived from the curve-of-growth (CoG) analysis, but also to analyse the fidelity of decomposition. Maps with relative residuals were also created for the same purpose, of checking the decomposition.

### 3.2 Sky determination and subtraction. Photometry

To derive the quantities necessary for the galaxy scaling relation analysis we had to calculate the integrated fluxes of the galaxies and their constituents. This requires accurate sky subtraction, because systematic errors in the derived sky background can propagate into significant uncertainties in the measured structural parameters. This can then bias the bulge-disk decomposition process towards unphysical and inaccurate results. This was realised in three successive steps.

**Step 1** We started the fitting process with the sky value as a free parameter, with an initial value obtained from the image outskirts. The exponential and Sérsic function parameters were left free as well. The input values for the coordinates of galaxy centre were determined after a careful inspection of each image. Position angles (PA) and axis-ratios were taken from NED (NASA/ IPAC Extragalactic Database).

Then, we ran GALFIT on the full rectangular area of the input image, masked for stars. We check whether the sky background value found by GALFIT is reasonable. This is necessary as experience shows that the Levenberg-Marquardt algorithm used by GALFIT can converge on a local minimum, giving inaccurate background values, when checked against the surface brightness profiles. This was done from a plot of the average surface brightness of the galaxy, calculated in elliptical annuli (the width of each annulus being 2 arcsecs) versus the semi-major axis radius. The profiles flatten to a non-zero level towards the edge of the image, beyond the radius at which there is no galaxy emission ( $R_{max}$ ). The mean value from this point is our estimate of the sky background. We noticed that the sky value found by GALFIT in this first run was not always corresponding to the zero galaxy emission level that one would expect. Therefore we subsequently used our determined sky value for those cases. We then plotted the sky-subtracted average surface brightness profile, superimposing the model fit and its components (bulge and disk), and the radius from which the elliptical annuli are incomplete ( $R_{2\sigma}$ ). Subsequently, we calculate and plot the curve-of-growth (CoG) along the semi-major axis-radius, with the background found in GALFIT subtracted, and overlay the

CoG for disk and bulge. We determine a preliminary value for the bulge-to-disk ratio ( $B/D$ ) from the disk and bulge CoGs. The  $B/D$  value is checked against the one determined by the ratio of the total counts of the decomposed disk and bulge images, because it should be consistent, within errors. From the corresponding CoGs, we determine preliminary values for the integrated fluxes of the galaxy, the disk and the bulge. The integrated flux of the galaxy is calculated from the maximum CoG value (in counts), at  $R_{max}$  radius (as stated above, this is the radius beyond which there is no galaxy emission and, therefore, the CoG is essentially flat toward larger radii). We use the exposure time and flux units conversion (PHOTFLAM) parameters present in the header of each galaxy image to convert the fluxes in Jy units. We then correct the fluxes for foreground extinction, to determine the intrinsic values.

**Step 2** In the second stage, we do a second run of GALFIT, this time with the sky background fixed to the value found from radial surface brightness profile inspection (**Step 1**). In most cases, it differs slightly from the value found by GALFIT, but it is more accurate and we noticed that these small differences can determine significant changes in the values of the output photometric parameters. As before, we plot the average surface brightness profile (calculated in elliptical annuli) of the observed galaxies, the model and the components versus semi-major axis radius, and the corresponding curves of growth (CoGs). We analyse the profiles and the fits, and then we determine again the  $B/D$  and the new values for the integrated fluxes of the galaxy, the disk and the bulge.

**Step 3** (where necessary) If the observed surface brightness profiles showed deviations from an exponential, due to noise or artifacts in the outskirts of the profiles, we create another mask. The new mask, an elliptical one, contained masked pixels beyond a certain radius ( $R_{mask}$ ) and the masked pixels from the original. It was used in a third run of GALFIT, with the background fixed to the 2nd run (Step 2) value and all the other parameters free. The whole process of plotting the surface brightness profiles, CoGs, and calculations of  $B/D$  and integrated fluxes is repeated as before. The uncertainties in the fluxes are estimated from the root mean square of the CoG values from the first 10 elliptical annuli beyond  $R_{max}$ . As in previous steps, the integrated flux of the galaxy is determined from the CoG value at  $R_{max}$ , and corrected for foreground extinction. Finally, after a careful inspection of all the profiles, CoGs, relative residuals, model and decomposed images, together with a check of the  $\chi^2$  values and the structural parameters, we decided which case (Step 1, 2 or 3) is the best fit to each observed galaxy image. Thus, the photometric and structural parameters for that case only (either Step 1, 2 or 3 fit) were retained and used further on in our study. For 7 sampled galaxies, we achieved a good fit at Step 1; for 4 of the others, a better result was found at Step 2; and for the remaining 7 galaxies, we found the best fit at Step 3. The derived integrated fluxes and bulge-to-disk ratios are given in Table 1, for the whole sample, together with distances to each galaxy used in this study, taken from NASA Extragalactic Database (NED).

We should mention here the very high derived  $B/D$  value for NGC4594 galaxy. This is an edge-on SAa type galaxy, with a huge bulge divided by the stellar and dust disks. Thus, the fitting procedure was more complicated, but both the observed and intrinsic values of the bulge-to-disk ratio are reasonable.

In Figs. 1 and 2 we show examples of the fitting steps for galaxies NGC3031 and NGC4826 to illustrate the whole procedure described here. For NGC3031, the observed average surface brightness profile was smooth up to  $R_{max}$ , without deviations from an exponential profile. Therefore, for this galaxy (as was the case

**Table 1.** The calculated fluxes for our sample (B band). The columns represent: (1) - galaxy name; (2) - distance to each galaxy, taken from NASA Extragalactic Database (NED), as derived in: *a* - Tully et al. (2013), *b* - Kreckel et al. (2017), *c* - Dalcanton et al. (2009), *d* - Jang et al. (2012), *e* - Mandel et al. (2011), *f* - Poznanski et al. (2009), *g* - Sorce et al. (2014) and *h* - McQuinn et al. (2016); (3) bulge-to-disk ratios (*B/D*) derived from the decomposed images, with systematic uncertainties, derived as described in Sec. 3.2; (4) - the integrated flux for each galaxy, in Jy; (5) - the error for the galaxy flux; (6), (7) - the integrated fluxes of the disk and bulge components, in Jy.

<i>Galaxy</i>	<i>d<sub>gal</sub></i> [Mpc]	<i>B/D</i>	<i>F<sub>gal</sub></i> [Jy]	$\sigma_{F_{gal}}$ [Jy]	<i>F<sub>d</sub></i> [Jy]	<i>F<sub>b</sub></i> [Jy]
NGC0024	7.67 <sup>a</sup>	0.00 <sup>+0.00</sup> <sub>-0.00</sub>	0.14	0.02	0.14	0.00
NGC0628	9.59 <sup>b</sup>	0.03 <sup>+0.00</sup> <sub>-0.00</sub>	1.34	0.01	1.30	0.04
NGC2841	14.60 <sup>a</sup>	0.19 <sup>+0.05</sup> <sub>-0.03</sub>	0.59	0.01	0.50	0.09
NGC2976	3.57 <sup>c</sup>	0.00 <sup>+0.00</sup> <sub>-0.00</sub>	0.37	0.01	0.37	0.00
NGC3031	3.62 <sup>d</sup>	0.61 <sup>+0.00</sup> <sub>-0.05</sub>	5.03	0.05	3.07	1.96
NGC3190	24.20 <sup>e</sup>	0.36 <sup>+0.02</sup> <sub>-0.08</sub>	0.25	0.01	0.18	0.07
NGC3621	6.73 <sup>a</sup>	0.05 <sup>+0.02</sup> <sub>-0.01</sub>	1.51	0.08	1.45	0.06
NGC3938	17.90 <sup>f</sup>	0.03 <sup>+0.00</sup> <sub>-0.00</sub>	0.31	0.01	0.30	0.01
NGC4254	14.40 <sup>f</sup>	0.15 <sup>+0.00</sup> <sub>-0.00</sub>	0.40	0.02	0.35	0.05
NGC4450	15.20 <sup>g</sup>	0.47 <sup>+0.08</sup> <sub>-0.06</sub>	0.31	0.04	0.22	0.09
NGC4594	9.55 <sup>h</sup>	4.14 <sup>+0.03</sup> <sub>-0.05</sub>	0.94	0.06	0.18	0.76
NGC4736	4.59 <sup>a</sup>	1.00 <sup>+0.03</sup> <sub>-0.02</sub>	1.29	0.02	0.64	0.65
NGC4826	5.50 <sup>g</sup>	0.04 <sup>+0.00</sup> <sub>-0.01</sub>	0.80	0.06	0.77	0.03
NGC5033	19.30 <sup>g</sup>	0.30 <sup>+0.01</sup> <sub>-0.02</sub>	0.33	0.06	0.25	0.08
NGC5055	8.20 <sup>g</sup>	0.16 <sup>+0.00</sup> <sub>-0.00</sub>	0.82	0.02	0.70	0.12
NGC5474	6.98 <sup>a</sup>	0.17 <sup>+0.03</sup> <sub>-0.02</sub>	0.10	0.01	0.08	0.01
NGC7331	13.90 <sup>a</sup>	0.27 <sup>+0.03</sup> <sub>-0.02</sub>	0.55	0.01	0.43	0.12
NGC7793	3.70 <sup>g</sup>	0.01 <sup>+0.00</sup> <sub>-0.00</sub>	1.47	0.02	1.46	0.01

for a few others in our sample), Step 3 fit was not necessary and the corresponding plots are not shown. However, for NGC4826 the situation was different, as it can be seen from the average surface brightness profile (black line), that there are deviations from an exponential disk profile inside  $R_{max}$ . Thus, a new mask was used, with all the pixels beyond  $R_{mask}$  excluded from the 3rd run fit.

We have used the positive sky residuals in the outer parts of galaxies (such as the one noticeable in the surface brightness profiles of NGC4826 or even NGC3031 towards  $R_{max}$  and beyond) to estimate the systematic errors in bulge-to-disk ratios. This is important as the sky level errors dominate the systematic errors in bulge-to-disk decompositions, as shown by Simard et al. (2002). These are shown in Table 1.

One could also use a 3rd function during the fitting procedure, to potentially improve the fit in the outskirts of some of the galaxies, as it would be the case for NGC4826 and a few other galaxies, when various features and deviations from an exponential disk are present, such as truncations / antitruncations, rings, noise etc. However, studying the outskirts of galaxies is beyond the purpose of the present paper, and we judge the 2-component fits to reproduce the surface brightness of the galaxies with sufficient fidelity in the region of interest for our study (at galactocentric radii up to 5 disk scalelengths).

Having obtained the best fit parameters (following the previously described procedure) and the integrated fluxes for the galaxies and their main components, we are in the position to calculate the central surface brightness (average effective surface brightness) for disks (bulges), together with the apparent and absolute magnitudes for both disks and bulges. Thus, following for example Gra-

ham & Driver (2005) or Graham & Worley (2008), for the disk central surface brightness we have

$$\mu_{0,d} = -2.5 \log\left[\frac{F_d}{2\pi(R_{s,d})^2 * Q_d}\right]/F_0 \quad (4)$$

where  $F_0$  is the zero point magnitude flux, used to convert  $\mu_0^d$  from units of  $Jy/arcsec^2$  to  $mag/arcsec^2$  (taken from the header of each .fits image),  $F_d$  is the disk flux (in Jy, see Table 1), while  $R_{s,d}$  and  $Q_d$  are the observed disk scalelength (in arcsecs) and axis ratio - derived using GALFIT.

The absolute and apparent disk magnitudes are obtained using the relations

$$M_d = m_d - 25 - 5 \log(d_{gal}/Mpc) \quad (5)$$

$$m_d = \mu_{0,d} - 2.5 \log(2\pi(R_{s,d})^2 * Q_d) \quad (6)$$

In a similar way we can write the equations for the bulge effective surface brightness, apparent and absolute magnitudes (see Graham & Driver 2005 or Graham & Worley 2008):

$$\mu_{e,b} = -2.5 \log\left[\frac{F_b}{2\pi(R_{e,b})^2 \exp(\kappa_n) n \kappa_n^{-2n} \Gamma(2n) Q_b}\right]/F_0 \quad (7)$$

where  $F_b$  is the integrated flux of the bulge,  $R_{e,b}$  is the effective radius (in arcsecs),  $\Gamma(2n) = 2\gamma(2n, \kappa_n)$ , with  $\Gamma$  and  $\gamma$  the complete and incomplete gamma functions (Graham & Driver 2005)

$$M_b = m_b - 25 - 5 \log(d_{gal}/Mpc) \quad (8)$$

$$m_b = \mu_{e,b} - 2.5 \log(2\pi(R_{e,b})^2 Q_b) - 2.5 \log\left[\frac{n \exp(\kappa_n) \Gamma(2n)}{\kappa_n^{2n}}\right] \quad (9)$$

We need to include the terms  $Q_d$  and  $Q_b$  - observed disk and bulge axis-ratios - in Eqs. 4&6 (for disks) and in Eqs. 7&9 (for bulges) as both disks and bulges are seen in projection, and we need to take this into account and correct for projection effects. Of course, as shown in Pastrav et al. (2013a), these effects are more pronounced for more inclined (close to edge-on) disks, where the disk thickness becomes relevant.

### 3.3 Dust opacity and dust mass derivation

We are now in the position to derive the dust central optical depth in B band -  $\tau_B^f$  and subsequently the dust mass ( $M_{dust}$ ) for each galaxy, having previously derived all the necessary quantities. In order to do this, we used the correlation between  $\tau_B^f$  and stellar mass surface density ( $\mu_*$ ) of nearby spiral galaxies, found by Grootes et al. (2013):

$$\log(\tau_B^f) = 1.12(\pm 0.11) \cdot \log(\mu_*/M_\odot kpc^{-2}) - 8.6(\pm 0.8) \quad (10)$$

The stellar mass surface density (expressed in units of  $M_\odot/kpc^2$ ) is derived using their Eq. 4, and replacing single Sérsic effective radius with the disk scale-length derived from bulge-disk decomposition, in that equation. This relation was obtained by analysing a sample of spiral galaxies taken from the Galaxy and Mass Assembly (GAMA) survey. Grootes et al. (2013) showed that with the values obtained through this correlation, they could successfully correct statistical samples of late-type galaxies for dust attenuation effects when only optical photometric data is available.

The stellar masses for our sample are not derived here (in fact being the only quantity involved in the galaxy scaling relations that we did not derive in this study) but taken from previous studies of KINGFISH/SINGS galaxies, such as those of Grossi et al. (2015),

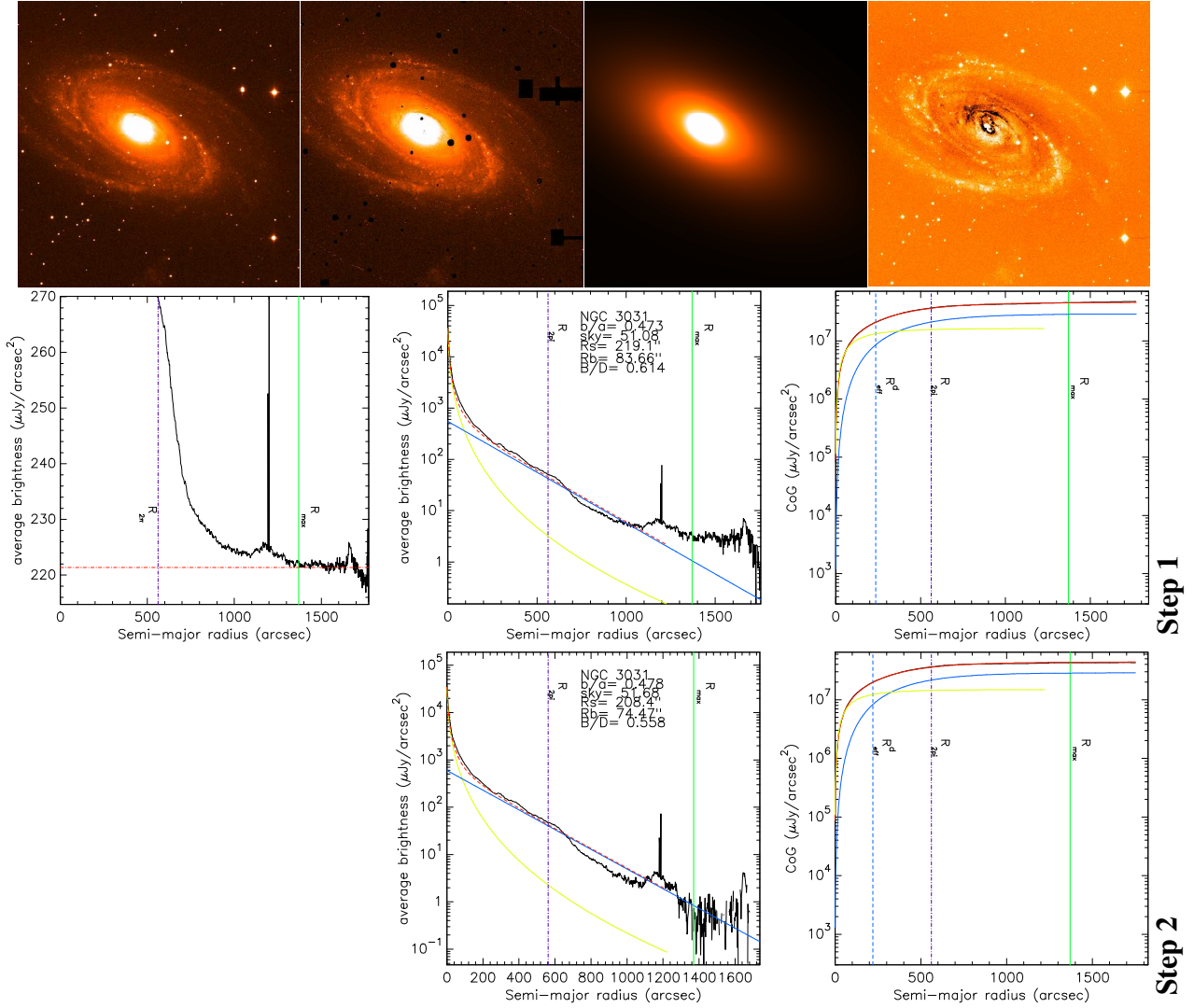


**Figure 1.** NGC3031 The panels are as follows: *Upper row* - the B band observed image, the masked observed image, the best model fit image and the absolute residuals image (e.g. data-fit), where very light colored regions/pixels represent positive residuals while dark ones correspond to negative ones; *Middle row* zoom of surface brightness profile in elliptical annuli - used to visually identify the background level (drawn as the red dot-dashed line), with  $R_{max}$  (radius of the maximum extent of emission in the galaxy) and  $R_{2\pi}$  (which denotes the major axis radius out to which data is available over the full azimuthal range) overplotted as vertical dashed dotted violet and green solid lines; surface brightness profiles and CoGs for the observed image (black), model image (the fit - red), disk (blue) and bulge (yellow), corresponding to Step 1, described in Sec. 3.2; *Lower row* surface brightness profiles and CoGs corresponding to Step 2. The angular size of the observed image on the sky is  $20.22' \times 20.54'$ . The vertical blue dashed line in the CoG plots show the position of the effective radius of the galaxy. Step 3 fit was not necessary for this galaxy.

Rémy-Ruyer et al. (2015), Skibba et al. (2011), Kennicutt et al. (2011) and Noll et al. (2009).

Using Eq. (2) from Grootes et al. (2013) (but see also Eqs. (A1-A5) from Appendix A of the same paper) shown here below, we derive the dust masses of each galaxy in our sample. This relation was calculated considering the dust geometry of the Popescu et al. (2011) model, where the diffuse dust in the disk (which mostly determines the optical depth of a spiral galaxy) is distributed axisymmetrically in two exponential disks.

$$\tau_B^f = K \frac{M_{dust}}{R_{s,d}} \quad (11)$$

where  $K = 1.0089 pc^2/kg$  is a constant containing the details of the dust geometry and the spectral emissivity of the Weingartner & Draine (2001) model, while  $R_{s,d}$  is the scale-length of the disk, expressed in kpc.

### 3.4 Correcting for dust, projection and decomposition effects

As we have already underlined in the first section of this paper, obtaining intrinsic structural and photometric parameters is essential when deriving accurate galaxy scaling relations.

To correct all the parameters involved we used the method developed and presented in Pastrav et al. (2013a,b). More specifically,

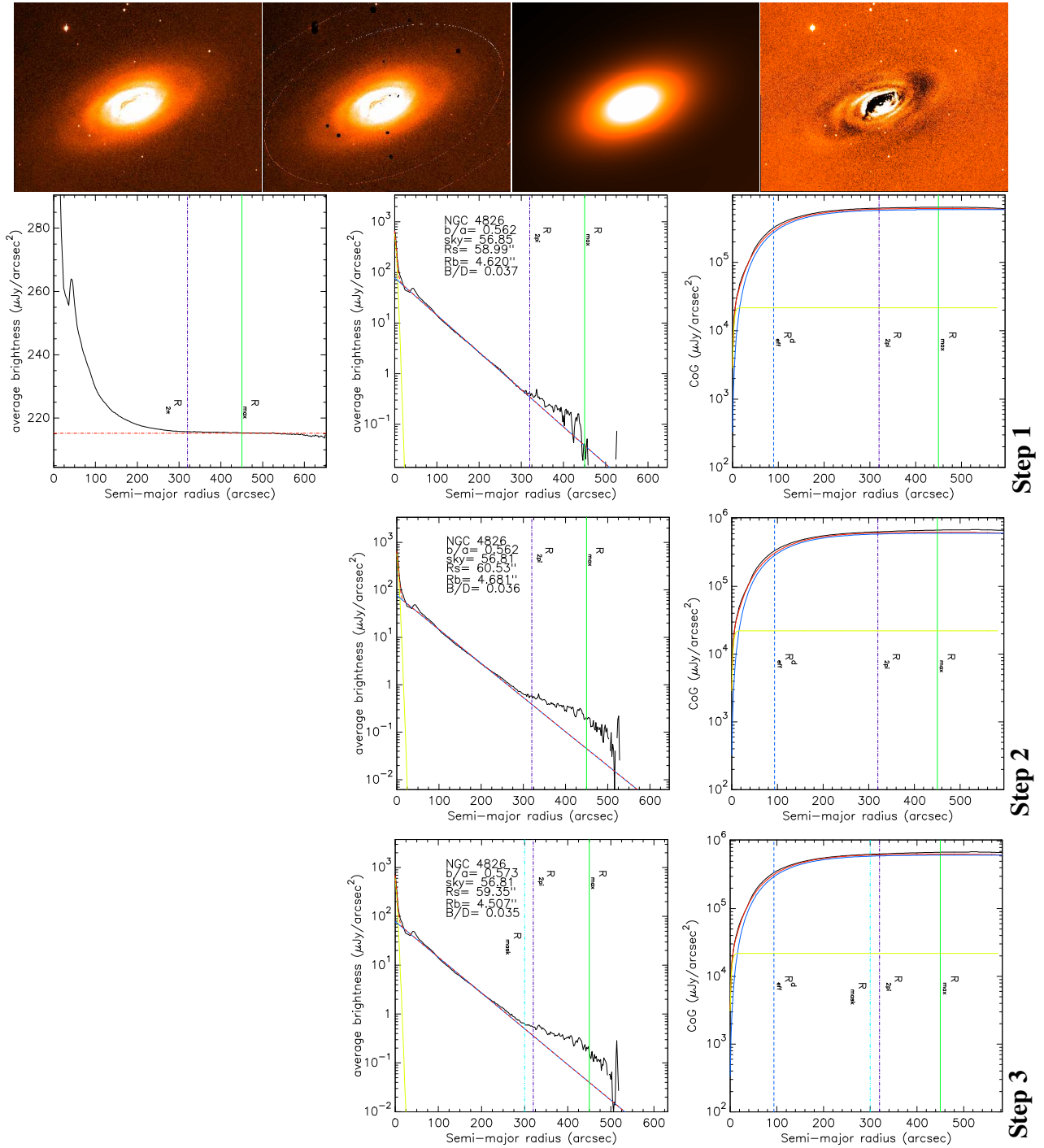


**Figure 2.** NGC4826 As for Fig. 1. Additionally, here the plots corresponding to Step 3 are shown on the 4th row - the surface brightness profiles and CoGs when an additional mask, setting the weight of all pixels beyond a semi-major radius of  $R_{mask}$  to zero is added (light blue vertical line). In the top row - 2nd panel from the left, the two dashed white ellipses denote  $R_{2\pi}$  (inner ellipse, the major axis radius out to which data is available over the full azimuthal range) and  $R_{max}$  (outer ellipse, the semi-major radius out to which emission from the galaxy could be detected). The angular size of the observed image on the sky is  $10.49' \times 8.03'$ .

we used the whole chain of corrections presented in Eqs. (4-13) from Pastrav et al. (2013a) and Eqs. (3-13) from Pastrav et al. (2013b), together with all the numerical results (given in electronic form as data tables at CDS) to correct the measured parameters for projection (inclination), dust and decomposition effects, in order to obtain their dust-free, intrinsic values.

Due to the fact that the numerical corrections are a function of

wavelength, dust opacity and/or bulge-to-disk ratio, we used the values of  $\tau_B^f$  and  $B/D$  already derived individually for each galaxy and did all the needed interpolations to obtain the final values for the structural and photometric parameters. Thus,  $Q_d$ ,  $R_{s,d}$ ,  $\mu_{0,d}$ ,  $m_{app,d}$ ,  $M_{abs,d}$  (for disk),  $B/D$ ,  $n$ ,  $R_{e,b}$ ,  $\mu_{e,b}$ ,  $m_{app,b}$ ,  $M_{abs,b}$  (for bulge) were fully corrected. Following from Eqs. 4-5, we calculate the in-

**Table 2.** Dust masses and dust opacities, derived using Eqs. 10 and 11. The different columns represent: (1) - galaxy name; (2) - B band face-on dust optical depth; (3) - stellar mass surface densities; (4) - corrected stellar mass surface densities; (5) - stellar masses taken from: *a* - Noll et al. (2009), *b* - Rémy-Ruyer et al. (2015), *c* - Grossi et al. (2015), *d* - Zibetti & Groves (2011), *e* - Skibba et al. (2011); (6) - dust masses; (7) - corrected dust masses; (8)-(11) - standard deviation for  $\tau_B^f$ ,  $\mu_*$ ,  $M_*$  and  $M_{dust}$ . The errors for the corrected quantities are the same and thus not given here. In square brackets we have the units in which these quantities are expressed. All quantities except dust optical depth are given in decimal logarithm unit scale.

<i>Galaxy</i>	$\tau_B^f$	$\log(\mu_*)$ [ $M_\odot/kpc^2$ ]	$\log(\mu_*^i)$ [ $M_\odot/kpc^2$ ]	$\log(M_*)$ [ $M_\odot$ ]	$\log(M_{dust})$ [ $M_\odot$ ]	$\log(M_{dust}^i)$ [ $M_\odot$ ]	$\sigma_{\tau_B^f}$	$\sigma_{\mu_*}$ [ $M_\odot/kpc^2$ ]	$\sigma_{M_*}$ [ $M_\odot$ ]	$\sigma_{M_{dust}}$ [ $M_\odot$ ]
NGC0024	2.59	8.05	8.76	9.65 <sup>a</sup>	6.76	6.50	0.48	0.07	0.07	0.09
NGC0628	1.64	7.87	8.46	10.29 <sup>b</sup>	7.38	7.25	0.26	0.06	0.06	0.07
NGC2841	5.89	8.37	9.24	10.85 <sup>c</sup>	8.00	7.58	0.92	0.06	0.06	0.07
NGC2976	3.01	8.11	8.75	9.13 <sup>c</sup>	6.25	6.05	0.60	0.08	0.07	0.10
NGC3031	3.80	8.59	9.28	11.00 <sup>a</sup>	8.18	7.50	0.40	0.04	0.04	0.05
NGC3190	4.71	8.28	9.02	10.58 <sup>c</sup>	7.72	7.43	0.73	0.06	0.06	0.07
NGC3621	3.35	8.15	9.13	10.05 <sup>c</sup>	7.18	6.64	0.53	0.06	0.06	0.07
NGC3938	3.06	8.11	8.89	10.45 <sup>c</sup>	7.57	7.25	0.48	0.06	0.06	0.07
NGC4254	5.92	8.37	9.25	10.60 <sup>c</sup>	7.75	7.32	0.92	0.06	0.06	0.07
NGC4450	7.81	8.48	9.25	10.80 <sup>d</sup>	7.97	7.64	2.02	0.10	0.10	0.11
NGC4594	3.80	9.23	10.09	10.97 <sup>c</sup>	8.23	6.66	0.61	0.06	0.06	0.07
NGC4736	3.80	9.21	9.83	10.33 <sup>c</sup>	7.58	6.28	0.66	0.07	0.06	0.09
NGC4826	5.56	8.34	9.42	9.99 <sup>e</sup>	7.14	6.51	1.74	0.12	0.12	0.14
NGC5033	1.18	7.74	8.27	10.77 <sup>a</sup>	7.85	7.77	0.33	0.11	0.11	0.12
NGC5055	3.46	8.16	8.98	10.62 <sup>c</sup>	7.75	7.38	0.54	0.06	0.06	0.07
NGC5474	0.62	7.49	7.96	9.06 <sup>c</sup>	6.11	6.09	0.08	0.05	0.05	0.08
NGC7331	4.96	8.30	9.07	10.99 <sup>c</sup>	8.13	7.82	0.77	0.06	0.06	0.07
NGC7793	1.75	7.89	8.62	9.47 <sup>c</sup>	6.57	6.29	0.28	0.06	0.06	0.08

trinsic disk central surface brightness as:

$$\mu_{0,d}^i = \mu_{0,d} - corr(\mu_{0,d}) - A_{ext} + A_{dim} \quad (12)$$

where  $A_{ext}$  is the attenuation due to the foreground galactic extinction (taken from NED, as in Schlafly & Finkbeiner 2011 recalibration of the Schlegel et al. 1998 infrared based dust map),  $corr(\mu_{0,d})$  is the total correction (due to dust and projection effects) for  $\mu_{0,d}$ , while  $A_{dim} = -2.5 \log(1+z)^3$  is the attenuation due to cosmological redshift dimming, per unit frequency interval.

The absolute and apparent disk magnitudes are corrected using the relations

$$M_d^i = m_d^i - 25 - 5 \log(d_{gal}/Mpc) \quad (13)$$

$$m_d^i = \mu_{0,d}^i - 2.5 \log(2\pi(R_{s,d}^i)^2 * Q_d^i) \quad (14)$$

where  $m_d^i$ ,  $R_{s,d}^i$  and  $Q_d^i$  are the intrinsic apparent disk magnitude, the intrinsic disk scalelength (in arcsecs) and axis-ratio.

In a similar way we can rewrite Eqs. 7-9 to calculate the intrinsic values for  $\mu_{e,b}$ ,  $m_b$  and  $M_b$  and obtain corresponding corrected scaling relations for bulges. However, those results will be detailed in a forthcoming paper.

All the galaxies in our sample are at low redshift and therefore we did not apply K-corrections or evolutionary ones. Correspondingly, the correction due to cosmological redshift dimming is also quite small, in the range 0.01 – 0.05 mag.

Moreover, as  $\mu_*$ ,  $M_{dust}$ ,  $M_{dust}/M_*$  do depend on the previously mentioned parameters (namely on  $R_{s,d}$ ), these quantities had to be corrected too for the aforementioned effects, by replacing the intrinsic parameters in the corresponding equations.

The values for all the previously mentioned parameters, for the disk, both the observed and the intrinsic ones, are shown in Tables 2 and 3, for the whole sample. We also give here the results for the bulge component - the measured (observed) ones - in Table 4.

### 3.5 Estimation of errors

The output best-fit parameters given by GALFIT suffer from an underestimation of uncertainties, as shown by Häussler et al. (2007). To estimate the errors on the main photometric parameters, we ran a new set of fits, for a few sampled galaxies. We fixed the sky value to the one found by GALFIT in Step 1 and added  $\pm 1\sigma$ , or  $\pm 3\sigma$  ( $\sigma$  being the uncertainty in the sky level), leaving all other parameters free. The systematic errors in the disk scalelengths and bulge effective radii were within the range 1-10 pixels (1-3 arcsecs). They were less significant for the axis-ratios, up to 0.01. Also, the random errors which occur in an exponential fit are < 10% (Maltby et al. 2012). The error over  $d_{gal}$  (measured distance to the galaxy) was taken from NED. Having the flux uncertainties already calculated (Table 1) we performed propagation of errors in Eqs. 4-5 and 10-14 to derive the standard deviations ( $\sigma$ ) for all the needed parameters. The respective values can be seen in Tables 2 and 3.

## 4 RESULTS

In this section, the main results of this study are presented. We concentrate on the scaling relations of the disks. The relations for the bulge component will be presented in a forthcoming paper, with scaling relations for elliptical galaxies. For three galaxies in our sample, namely NGC3031, NGC4594 and NGC4736, the initial value derived for  $\tau_B^f$  is higher than 8.0 - the upper limit of the numerical corrections for dust effects given in Pastrav et al. (2013a) and Pastrav et al. (2013b). These values are unrealistically large. This could be due to either an overestimate of the stellar mass, or issues with the fit/sky determination (especially for the case of NGC4594) resulting in a larger value for  $R_{s,d}$ . Therefore, for these 3 galaxies we have chosen to fix the value of the dust opacity to 3.80 (see Table 2), the average value found by Driver et al. (2007). However, this does not significantly change the overall trends we

**Table 3.** The photometric and structural parameters of the disks. The columns represent: (1) - galaxy name; (2) - the intrinsic disk axis-ratio, corrected for inclination (projection) effects and dust effects; (3), (4) - the observed and intrinsic disk scalelengths; (5) - intrinsic bulge-to-disk ratio; (6-8) - the observed, the intrinsic disk central surface brightness, and the standard deviation; (9-11) - the observed, the intrinsic apparent disk magnitude, and the standard deviation; (12-14) - the observed, the intrinsic disk absolute magnitude, and the standard deviation. In square brackets we have the units in which these quantities are expressed.

<i>Galaxy</i>	$Q_d^i$	$R_{s,d}$ [kpc]	$R_{s,d}^i$ [kpc]	$(B/D)^i$	$\mu_{0,d}$ [ $\frac{\text{mag}}{\text{arcsec}^2}$ ]	$\mu_{0,d}^i$ [ $\frac{\text{mag}}{\text{arcsec}^2}$ ]	$\sigma_{\mu_{0,d}}$	$m_d$ [mag.]	$m_d^i$ [mag.]	$\sigma_{m_d}$	$M_d$ [mag.]	$M_d^i$ [mag.]	$\sigma_{M_d}$
NGC0024	0.24	1.66	1.11	0.00	19.70	17.18	1.85	11.17	9.36	1.88	-18.25	-20.07	1.97
NGC0628	0.95	3.61	3.29	0.03	20.33	19.64	0.54	8.79	8.45	0.55	-21.12	-21.46	0.58
NGC2841	0.51	4.15	2.54	0.20	19.97	17.23	0.79	9.85	8.19	0.80	-20.97	-22.63	0.87
NGC2976	0.57	0.74	0.62	0.00	19.38	17.34	1.03	9.92	8.38	1.05	-17.84	-19.39	1.13
NGC3031	0.47	3.73	2.90	0.63	20.74	18.31	0.59	7.86	6.04	0.60	-19.94	-21.76	0.69
NGC3190	0.39	3.35	2.40	0.40	19.17	16.38	1.74	10.88	8.84	1.77	-21.04	-23.08	1.79
NGC3621	0.44	2.11	1.15	0.04	18.87	16.53	0.73	8.67	7.69	0.74	-20.47	-21.45	0.80
NGC3938	0.92	3.50	2.42	0.03	20.32	19.14	1.03	10.38	10.01	1.05	-20.88	-21.26	1.18
NGC4254	0.78	3.10	1.89	0.16	20.18	17.92	0.95	10.22	9.03	0.97	-20.58	-21.77	1.26
NGC4450	0.69	3.46	2.37	0.49	20.72	17.96	1.43	10.77	8.83	1.45	-20.14	-22.08	1.65
NGC4594	0.11	1.50	1.10	4.21	18.43	13.53	2.16	10.94	7.41	2.21	-18.96	-22.49	2.24
NGC4736	0.72	1.35	0.71	1.05	19.31	17.72	1.03	9.69	8.53	1.05	-18.62	-19.78	1.13
NGC4826	0.57	1.58	0.77	0.04	19.63	17.04	0.76	9.36	8.36	0.78	-19.34	-20.34	0.86
NGC5033	0.43	7.03	7.12	0.31	21.41	20.61	0.92	10.72	10.12	0.94	-20.71	-21.31	1.14
NGC5055	0.49	3.56	2.63	0.15	20.75	18.73	0.58	9.46	8.39	0.60	-20.11	-21.18	0.90
NGC5474	0.97	0.96	1.42	0.16	21.92	21.83	1.09	11.80	11.75	1.11	-17.41	-17.47	1.27
NGC7331	0.36	5.38	3.66	0.29	20.38	17.19	0.76	9.99	7.62	0.77	-20.72	-23.09	0.85
NGC7793	0.64	1.48	1.06	0.01	19.74	19.02	0.57	8.67	8.63	0.59	-19.18	-19.21	0.67

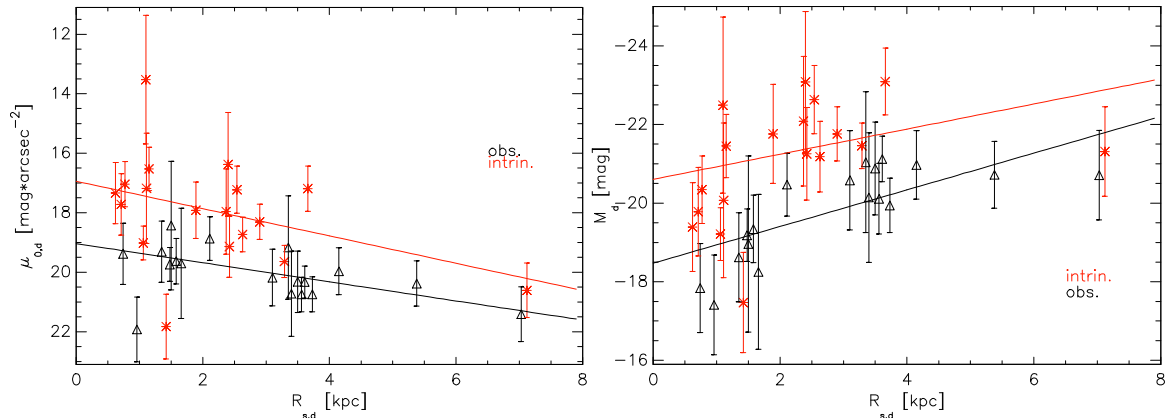


**Figure 3.** Left panel: Central disk surface brightness versus disk scalelength. Right panel: Disk magnitude versus disk scalelength. The black triangles represent the measured (observed) values, while the red crosses are the intrinsic (corrected for inclination, dust and decomposition effects) values. The black and red solid lines are obtained from a linear regression fit to the data points. The error bars represent the standard deviations.

observe or the mean values for  $\tau_B^f$  and dust/stellar ratios, even if we exclude these galaxies from calculations.

First, in Fig. 3 we show the brightness-size and size-luminosity relations for disks in our sample, in the form of central surface brightness vs. disk scale-length (left panel) and absolute magnitude vs. disk scalelength (right panel). For both cases, we show the observed values (black triangles) and the intrinsic ones (red crosses), fully corrected. One can notice from the left panel plot a displacement of the corrected values with respect to the measured ones to the left, towards smaller scalelengths, and upwards, towards higher central surface brightness values. This is expected because it was shown in Pastrav et al. (2013a) how dust biases the disk measurements towards larger scalelengths and fainter central surface brightness values compared with the real (intrinsic) values, with projection and decomposition effects

having smaller contributions. The same argument explains the similar behaviour of observed vs. intrinsic parameters seen in the right panel of Fig. 3. As one can see from both Table 3 and Fig. 3 (left panel), the decrease in central surface brightness is very strong as a result of applying the corrections - up to 2 mag. or more in some cases. The corresponding changes in the values of  $M_d$  are also quite large, but not as significant as for  $\mu_{0,d}$ . These differences are more significant than in previous similar studies, such as that of Graham & Worley (2008) for example.

The solid black and red lines represent linear regression fits to the observed and intrinsic data points. Applying the aforementioned corrections produces a slope change for both relations displayed in Fig. 3. Specifically, for the  $\mu_{0,d} - R_{s,d}$  relation, the slope changes from  $0.32 \pm 0.07$  to  $0.45 \pm 0.15$ , while for the  $M_d - R_{s,d}$  relation the slope decreases from  $-0.46 \pm 0.10$  to  $-0.32 \pm 0.14$ . The

**Table 4.** The photometric and structural parameters of the bulges. The columns represent: (1) - galaxy name; (2) - the observed bulge axis-ratio; (3) - the observed effective radii; (4) - (5) - the derived effective surface brightness and absolute bulge magnitudes; (6) - bulge Sérsic index.

Galaxy	$Q_b$	$R_{e,b}$ [kpc]	$\mu_{e,b}$ [ $\frac{\text{mag.}}{\text{arcsec}^2}$ ]	$M_b$ [mag.]	$n$
NGC0024	0.00	0.00	0.00	0.00	0.00
NGC0628	0.92	0.45	20.19	-17.34	1.17
NGC2841	0.66	0.69	19.06	-19.13	1.50
NGC2976	0.00	0.00	0.00	0.00	0.00
NGC3031	0.70	1.47	20.84	-19.45	3.20
NGC3190	0.27	1.53	18.54	-19.96	0.56
NGC3621	0.53	1.15	21.29	-17.01	0.15
NGC3938	0.94	0.45	20.22	-17.19	0.86
NGC4254	0.79	1.65	21.97	-18.46	2.02
NGC4450	0.62	2.18	21.75	-19.33	3.63
NGC4594	0.75	21.31	25.87	-20.53	4.76
NGC4736	0.90	0.27	17.89	-18.66	1.60
NGC4826	0.66	0.12	18.28	-15.82	0.78
NGC5033	0.40	1.76	20.18	-19.46	1.34
NGC5055	0.62	1.32	21.21	-18.19	1.10
NGC5474	0.77	1.04	23.82	-15.51	1.72
NGC7331	0.39	1.25	19.35	-19.24	0.71
NGC7793	0.85	0.03	17.73	-13.76	1.33

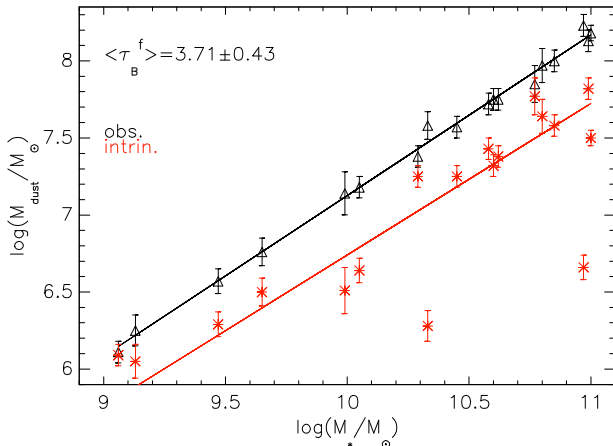


**Figure 4.** The galaxy dust mass (calculated using Eq. 11) versus galaxy stellar mass. The black triangles represent the measured (observed) values, while the red crosses are the intrinsic (corrected for inclination, dust and decomposition effects) values. The black and red solid lines are obtained from a linear regression fit to the data points. The mean value of the B band central optical depth is shown on the plot. The error bars represent the standard deviations.

value of 0.32 is close to the average ones of 0.32 and 0.35 found by Courteau et al. (2007) for the size-luminosity relations in I band and K bands, from an extensive analysis of global structural parameters of field and cluster spiral galaxies. Courteau et al. (2007) showed that the slope of size-luminosity relation varies strongly with morphology of the spiral galaxies, with early types having smaller scalelengths than late type spirals. Our sample is too small to examine this behaviour.

We present in Fig. 4 an important scaling relation for galaxy and ISM evolution studies, the dust mass (calculated from Eq. 11) versus the stellar mass relation. We recover the trend already ob-

served in other studies of disk scaling relations, a linear increase of the dust mass as we go towards galaxies with higher stellar masses. Since the dust mass as expressed in Eq. 11 depends on a parameter which is affected by dust, inclination and decomposition effects -  $R_{s,d}$ , we also show in red the same relation with the corresponding corrections applied. Similar to the first two relations, we find the best fit (solid black and red lines) from a linear regression procedure applied to the observed and corrected values. The slope of  $M_{dust} - M_*$  is close to unity for the observed relation -  $1.04 \pm 0.02$ , with a small decrease for the corrected one ( $0.98 \pm 0.14$ ). It is also seen that for NGC4594 and NGC4736 the intrinsic dust masses are far from the intrinsic relation and their observed values. This could be due to our assumption for the dust opacity  $\tau_B^f = 3.80$ . Overall, an increase in the scatter from the observed to intrinsic relation is noticeable. This can be explained by the uncertainty involved in deriving an accurate value for the dust optical depth (it is a quantity which in general is difficult to be determined with great precision) or the underestimation of errors for the stellar mass (taken from the source papers mentioned in Table 2), dust opacity and disk scale-length.

One important result that we should mention here is the B band face-on mean opacity of disks derived for the entire sample (displayed on the plot) from the values in Table 2:  $\tau_B^f = 3.71 \pm 0.43$ . This is a value consistent with other studies of dust attenuation in spiral galaxies. For example, Driver et al. (2007) found a value of  $3.8 \pm 0.7$  by studying the empirical attenuation - inclination relation in B band for a large sample of 10095 galaxies from the Millennium Galaxy Catalog (MCG), result which agrees well with the theoretical predictions of dust attenuation versus inclination as a function of  $\tau_B^f$  from Tuffs et al. (2004).

In connection with the previous plot, in Fig. 5 are plotted the dust-to-stellar mass ratio versus stellar mass relation (left panel), while in the right panel the dust-to-stellar mass ratio is plotted as a function of stellar mass surface density,  $\mu_*$ . As one can see from both plots, the variation of  $M_d/M_*$  with stellar mass or  $\mu_*$  shows a flat, slightly increasing trend. However, after correcting all the parameters involved in these scaling relations (except  $M_*$ ) for the previously mentioned effects, we see how the dust-to-stellar mass ratio anti-correlates with both the stellar mass and stellar mass surface density. These trends are not new and have been previously discovered in larger observational studies by Cortese et al. (2012) and da Cunha et al. (2010), the latter in the form of a  $M_d/M_* - sSFR$  relation ( $sSFR = SFR/M_*$  - specific star formation rate). Grossi et al. (2015) confirmed this behaviour for the dust/stellar mass ratio as a function of stellar mass from a study of Virgo cluster galaxies and KINGFISH spirals, among others. As da Cunha et al. (2010) explained, the trend seen in Fig. 5 is a consequence of the  $sSFR$  variation with stellar mass. Thus, for low stellar mass galaxies that have high  $sSFR$  and gas fractions, a large amount of dust is formed, exceeding the dust quantity destroyed by various processes in the ISM. When we go towards more massive galaxies (e.g. earlier morphologies, higher  $M_*$ ), both the specific star formation rate and gas fraction decrease, and so the newly formed dust can no longer overcome the destroyed mass of dust. This should explain why  $M_d/M_*$  decreases with stellar mass and the surface density of the stellar mass.

In all the previously mentioned studies, the observed decrease of the dust-to-stellar mass ratio with stellar mass is slightly more pronounced than ours. This is due to the samples being analysed in the respective studies spanning more orders of magnitude in stellar mass. The fact that we notice the expected trends in Fig. 5 only after applying the corrections suggest that at least at short wavelengths

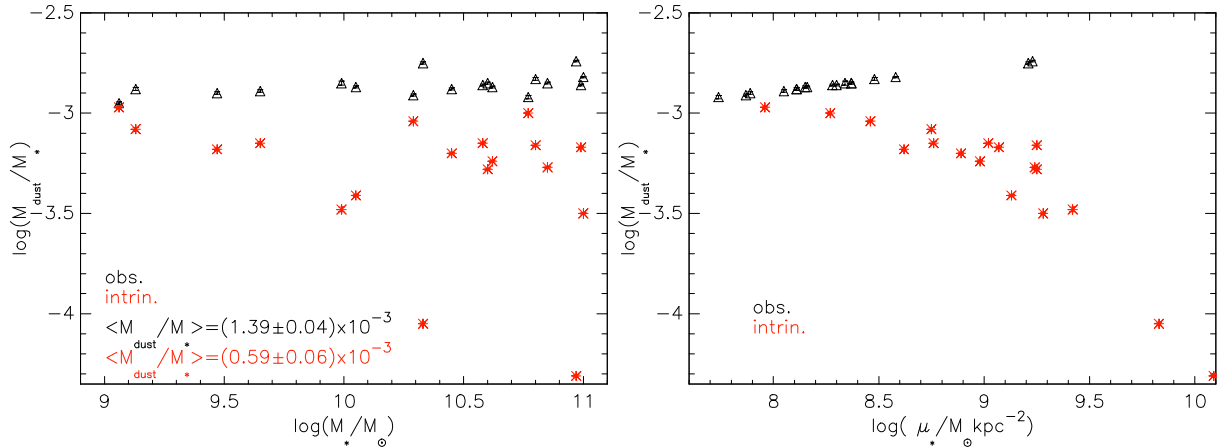


**Figure 5.** Left panel: Dust to stellar mass ratio, versus galaxy stellar mass. Right panel: Dust to stellar mass ratio versus stellar surface density. The black triangles represent the measured (observed) values, while the red crosses are the intrinsic (corrected for inclination, dust and decomposition effects) values. The average observed and corrected values for the dust to stellar mass ratio are shown on the left panel plot. The error bars represent the standard deviations.

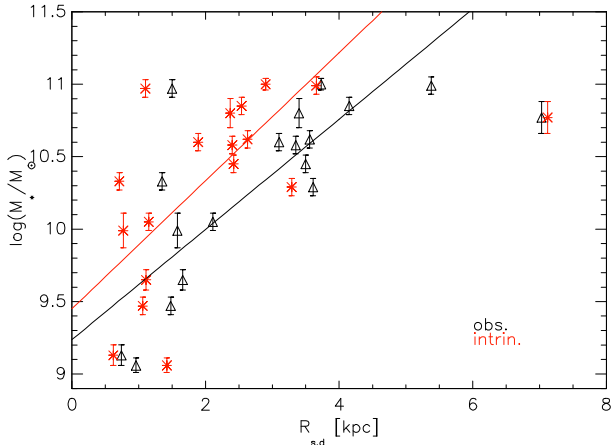


**Figure 6.** The galaxy stellar mass as a function of disk scalelength. The symbols and solid lines follow the same convention as in previous plots.

observational results can be biased and lead to wrong conclusions. Therefore, we caution that when these quantities do depend on dust biased quantities, the necessary corrections should be applied to the measured quantities.

In addition, we derive the mean dust-to-stellar mass ratio for the galaxies in our sample, and display both the observed and corrected values on the left panel plot in Fig. 5. The measured value of  $(1.39 \pm 0.04) \times 10^{-3}$  ( $-2.85$  in log scale) agrees very well with the value  $\log(M_d/M_*) = -2.83 \pm 0.08$  determined by [Skibba et al. \(2011\)](#) for all the spirals from the KINGFISH survey (see their Table 2). Our value (and the decreasing trend) is also consistent with the value of  $-3.03$  found by [Calura et al. \(2017\)](#) (see their Table 2) for the KINGFISH spirals, and the value  $2.0 \times 10^{-3}$  derived by [Dunne et al. \(2011\)](#) for low redshift galaxies from the H-ATLAS survey.

[Skibba et al. \(2011\)](#) calculated the dust mass using the dust temperature derived from modified blackbody fits to the far-infrared spectral energy distribution of each galaxy, a completely different method to that used in this study. Even so, our results are consistent with those obtained in that study for the mean observed dust-to-stellar mass ratio. The corrected mean value,  $(0.59 \pm 0.06) \times 10^{-3}$

( $-3.23$  in log scale), is significantly lower than the measured one, and the one found by [Skibba et al. \(2011\)](#).

Another scaling relation that we show in this study is the stellar mass - size relation, in Fig. 6. We recover the expected trend - the decimal logarithm of the stellar mass increases linearly with disk scalelength, e.g. more massive galaxies have more extended stellar disks. We do not correct the stellar masses for dust effects, only the disk scalelengths. The corrected relation shows a more accentuated increase of the stellar mass with disk size. This could be caused by the fact that  $M_*$  values were not corrected to the intrinsic ones. However, considering that we used stellar mass values from different studies determined using various methods, it was not straightforward to apply corrections because for certain wavelengths / emission lines these are simply not available (see [Pastrav et al. 2013a](#), [Pastrav et al. 2013b](#)). But we emphasize that the respective luminosities or nebular / emission line fluxes are affected by dust, to a larger or lesser extent. Nevertheless, obtaining an accurate mass - size relation is important for galaxy evolution studies.

## 5 DISCUSSION

One important feature of any scaling relation is its scatter, which a successful model of galaxy evolution should be able to reproduce, and the zero point and the slope of the relation. The cause of the low scatter in scaling relations such as Tully-Fisher, Faber Jackson and others is still not fully established. A contribution to this scatter may come from inaccurately derived parameters involved in these relations (due to fitting limitations of each galaxy) or not taking into account biases introduced by dust. In this respect, we analyse the size-luminosity relation to see if applying dust and inclination corrections produce either a reduction or an increase in the scatter of the intrinsic relation compared to the observed one. Specifically, we analyse the scatter of the surface brightness - scalelength or equivalently, of the absolute magnitude - scalelength relations. For this purpose, we calculate the residuals: the observed (intrinsic) values minus the linear regression fit to the observed (intrinsic) values. The corresponding values are presented in Fig. 7, with the corresponding uncertainties overplotted.

As one can see from both plots, there is a very mild dependence of the residuals on the central surface brightness (absolute magnitude). However, taking into account the uncertainties and leaving

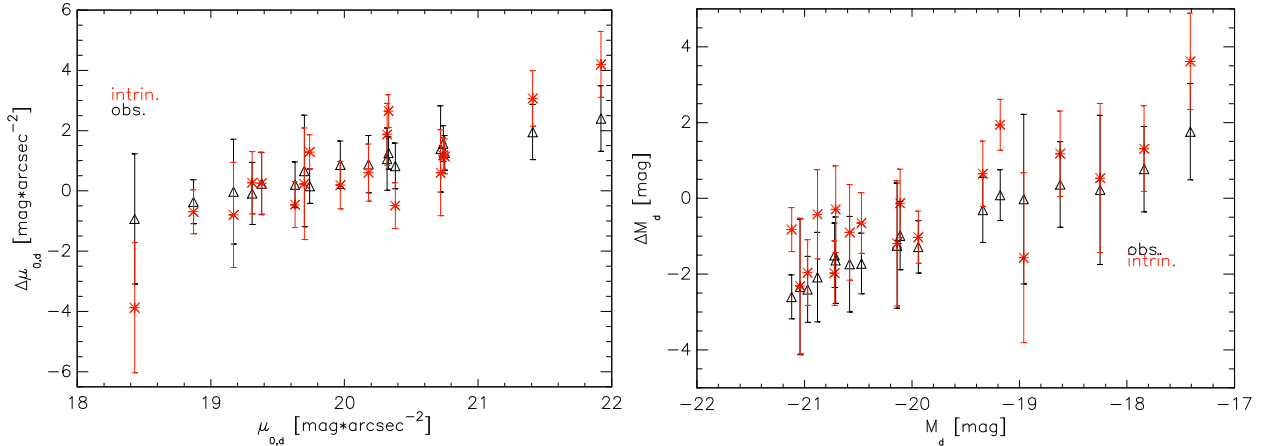


**Figure 7.** Left panel: Residuals, between observed central disk surface brightness values and the linear regression fit to the observed central disk surface brightness - disk scalelength relation (see Fig. 3), in black color; in red color, the same but for the intrinsic case. Right panel: The same, but for the disk absolute magnitude - disk scalelength relation. The symbols are the same as in previous plots.

out the two data points which are far out from the fits also in Figs. 3-6, one cannot observe a clear decrease or increase in the scattering of these relations when going from the observed to the intrinsic ones. At longer wavelengths we expect to have even flatter trends in the variation of the residuals with central surface brightness (absolute magnitude), as the combined effects of dust and inclination are less pronounced.

We also test the correlation for  $\mu_{0,d} - R_{s,d}$  and  $M_d - R_{s,d}$  relations by calculating the Pearson correlation coefficients. Thus, for the surface brightness - size relation we get  $r = 0.46$  for the measured values and  $r = 0.42$  for the intrinsic ones, while for the magnitude - size relation we obtain Pearson coefficients of  $-0.76$  and  $-0.40$ . As the coefficients for the measured relations are closer to 1 or -1 than the ones for the corrected relations, it appears that at this level, eliminating the bias introduced by projection, dust and decomposition effects produces less correlated size-luminosity relations and the scatter is increased. However, we need to take into consideration that our sample is quite small and limited to nearby (low redshift) galaxies.

If we were to analyse a similar sample of spiral galaxies at higher redshifts but at same wavelength, in order to assess how these relations would change, we would notice that the disk scalelengths would be smaller considering an inside-out scenario of galaxy evolution. Correspondingly, the disk central surface brightness and magnitude will be higher as we go towards higher redshifts. This has been shown by Barden et al. (2005), by analysing the surface brightness and surface mass density evolution of a sample of disk galaxies from the GEMS (Galaxy Evolution from Morphology and SEDs) survey, in V band and at redshifts up to  $z = 1.1$ . Barden et al. (2005) find a 1 mag increase in magnitudes and central surface brightness by  $z = 1$ .

## 6 SUMMARY AND CONCLUSIONS

We presented here the results of a study of the combined effects of dust, inclination and decomposition effects on some of the scaling relations of nearby spiral galaxies. We have done a detailed analysis of a sample of 18 typical unbarred spiral galaxies taken from the KINGFISH survey, in B band, representative for the nearby universe galaxies. A careful surface photometry and

sky determination and subtraction was performed to derive the integrated fluxes of each galaxy and its main components - disks and bulges. We derived the measured (observed) photometric and structural parameters of disks and bulges by doing a 2-component bulge-disk decomposition of galaxies, using GALFIT data analysis algorithm. Prior to fitting, a customized mask was applied to each galaxy image to take out all the bad pixels corresponding to nearby stars/galaxies, image artifacts, negative pixels and noise. Together with the integrated fluxes and the structural parameters, we calculated the central surface brightness and absolute magnitude for disks and bulges of each galaxy, and the bulge-to-disk ratios.

Using Grootes et al. (2013) empirical relation (Eq. 10), we have derived the central face-on dust opacities in B band ( $\tau_B^f$ ), and subsequently the dust mass of each galaxy, using Eq. 11 - obtained considering the dust geometry of Popescu et al. (2011) model. Using the numerical corrections for projection, dust and decomposition effects determined in Pastrav et al. (2013a) and Pastrav et al. (2013b) we corrected all the necessary photometric and structural parameters to obtain their intrinsic values. We then presented disk scaling relations, such as central surface brightness - scalelength, magnitude - scalelength, dust vs stellar mass, dust-to-stellar ratios vs. stellar mass/ stellar mass surface density, or stellar mass as a function of disk scalelength. Both the observed (measured) and the intrinsic (corrected) relations were presented, corrected for all the aforementioned effects, in order to better illustrate the differences in the overall trend, in their slopes and zero points. By analysing these relations, our main conclusions are:

- for the size-luminosity type of relations (Fig. 3), the decrease in central surface brightness is important as a result of applying the corrections - up to 2 mag. or more, in some cases; the corresponding changes in the values of  $M_d$  are also quite large, but not as much as for  $\mu_{0,d}$
- the slope of the  $\mu_{0,d} - R_{s,d}$  relation changes from 0.32 (observed) to 0.45 (intrinsic), while for the  $M_d - R_{s,d}$  relation the slope decreases from  $-0.46$  to  $-0.32$ , when corrections are applied; the slopes for the observed relations are similar with those found in other studies of spiral galaxies
- the slope of  $M_{dust} - M_*$  is close to unity for the observed relation -  $1.04 \pm 0.02$ , with a small decrease for the corrected one ( $0.98 \pm 0.14$ )

- the mean value for the central face-on dust opacity that we find for our small sample -  $\tau_B^f = 3.71 \pm 0.43$ , is consistent with other studies of dust attenuation in spiral galaxies, done on much larger samples, such as the one of [Driver et al. \(2007\)](#)

- we recover the expected trends in the dust-to-stellar mass ratio as a function of stellar mass / stellar surface density (Fig. 5) only after applying the necessary corrections, which comes to underline the importance of having unbiased, dust free scaling relations

- the mean value of the observed dust-to-stellar mass ratio of our sample,  $(1.39 \pm 0.04) \times 10^{-3}$  ( $-2.85$  in log scale) is in very good agreement with the mean value  $\log(M_d/M_*) = -2.83 \pm 0.08$  found by [Skibba et al. \(2011\)](#) for all the spirals from the same KINGFISH survey, using a completely different method; the intrinsic value,  $(0.59 \pm 0.06) \times 10^{-3}$  ( $-3.23$  in log scale), is lower than the measured one, and the one found by [Skibba et al. \(2011\)](#)

- the intrinsic size-luminosity relations show a larger scatter than the observed ones, while the correlations are not so strong

We have chosen to do this study in B band as our method is useful when optical data is available, but also because we can see more clearly the changes in the scaling relations at shorter wavelengths, when dust effects are stronger. Thus, the method presented here, to obtain intrinsic scaling relations, is tailored for cases where optical data is available. In this paper we have concentrated on disk scaling relations and spiral galaxies. In a future paper, we will show corresponding results for bulges and elliptical galaxies.

## ACKNOWLEDGEMENTS

We would like to thank the referee, Stephen Serjeant, for a careful reading of the manuscript and for the useful suggestions which improved the quality and clarity of this paper. This research made use of the NASA/IPAC Extragalactic Database (NED), which is operated by the Jet Propulsion Laboratory, California Institute of Technology, under contract with the National Aeronautics and Space Administration.

The author would like to acknowledge financial support from the project Nucleu - LAPLAS VI.

## REFERENCES

Barden, M., Rix, H.-W., Somerville, R. S. et al. 2005, *ApJ*, 635, 959  
 Bourne, N., Maddox, S. J., Dunne, L. et al. 2012, *MNRAS*, 421, 3027  
 Byun Y. I., Freeman K. C., Kylafis N. D. 1994, *ApJ*, 432, 114  
 Calura, F., Pozzi, F., Gresci, C. et al. 2017, *MNRAS*, 465, 54  
 Ciotti, L. & Bertin, G. 1999, *A&A*, 352, 447  
 Cortese, L., Ciesla, L., Boselli, A. et al. 2012, *A&A*, 540, A52  
 Courteau, S., Dutton A. A., van den Bosch, F. C. et al. 2007, *ApJ*, 671, 203  
 Cunow B. 2001, *MNRAS*, 323, 130  
 da Cunha, E., Eminian, C., Charlot, S., Blaizot, J. 2010, *MNRAS*, 403, 1894  
 Dalcanton, J. J., Williams, B. F., Seth, A. C. et al. 2009, *ApJS*, 183, 67  
 Dale, D. A., Aniano, G., Engelbracht, C. W., et al. 2012, *ApJ*, 745, 95  
 Dariush, A., Cortese, L., Eales, S., et al. 2011, *MNRAS*, 418, 64  
 Devour, B. M., Bell, E. F. 2017, *MNRAS*, 468, L31  
 Djorgovski, S. & Davis, M. 1987, *ApJ*, 313, 59  
 Driver, S. P., Popescu, C. C., Tuffs, R. J. et al. 2007, *MNRAS*, 379, 1022  
 Dunne, L., Gomez, H. L., da Cunha, E., et al. 2011, *MNRAS*, 417, 1510  
 Evans R. 1994, *MNRAS*, 266, 511  
 Faber, S. M. & Jackson, R. E. 1976, *ApJ*, 204, 668  
 Finkbeiner, D. P., Davis, M., Schlegel, D. J. 1999, *ApJ*, 524, 867  
 Gadotti A. D., Baes M., Falony S. 2010, *MNRAS*, 403, 2053  
 Graham, A.W. & Driver, S.P. 2005, *PASA*, 22, 118  
 Graham, A. W. & Worley, C. C. 2008, *MNRAS*, 388, 1708

Grossi, M., Hunt, L. K., Madden, S. C. et al. 2015, *A&A*, 574, A126  
 Grootes, M., Tuffs, R.J., Popescu, C.C. et al. 2013, *ApJ*, 766, 59  
 Häußler, B., McIntosh, D. H., Barden, M. et al. 2007, *ApJS*, 172, 615  
 Jang, I. S., Lim, S., Park, H. S., Lee, M. G. 2012, *ApJL*, 751, 19  
 Kennicutt, R. C., Armus, L., Bendo, G. et al. 2003, *PASP*, 115, 928  
 Kreckel, K., Groves, B., Bigiel, F. et al. 2017, *ApJ*, 834, 174  
 Kormendy, J. 1977, *ApJ*, 218, 333  
 Kennicutt, R. C., Calzetti, D., Aniano, G. et al. 2011, *PASP*, 123, 1347  
 Laurikainen E., Salo H., Buta R. et al. 2006, *AJ*, 132, 2634  
 Maltby, D. T., Gray, M. E., Aragón-Salamanca, A. et al. 2012, *MNRAS*, 419, 669  
 Mandel, K. S., Narayan, G., Kirshner, R. P. 2011, *ApJ* 731, 120  
 McQuinn, B. K., Skillman, E. D., Dolphin, A. E., Berg, D., Kennicutt, R. 2016, *AJ*, 152, 144  
 Möllenhoff, C., Popescu, C. C., Tuffs, R. J. 2006, *A&A*, 456, 941  
 Noll, S., Burgarella, D., Giovannoli, E. et al. 2009, *A&A*, 507, 1793  
 Pastrav, B. A., Popescu, C. C., Tuffs, R. J., Sansom, A. E., 2013a, *A&A*, 553, A80  
 Pastrav, B. A., Popescu, C. C., Tuffs, R. J., Sansom, A. E. 2013b, *A&A*, 557, A137  
 Planck Collaboration 2016, *A&A*, 594, A13  
 Peng, C. Y., Ho, L. C., Impey, C. D., Rix, H.-W. 2002, *AJ*, 124, 266  
 Peng, C. Y., Ho, L. C., Impey, C. D., Rix, H.-W. 2010, *AJ*, 139, 2097  
 Popescu, C. C., Misiriotis, A., Kylafis, N. D., Tuffs, R. J. & Fischera, J. 2000, *A&A*, 362, 138  
 Popescu, C.C., Tuffs, R.J., Völk, H.J., Pierini, D., Madore, B.F. 2002, *ApJ*, 567, 221  
 Popescu, C. C., Tuffs, R. J., Dopita, M. A. et al. 2011, *A&A*, 527, A109  
 Poznanski, D., Butler, N., Filippenko, A. V. et al. 2009, *ApJ*, 694, 1067  
 Schlafly, E. F. & Finkbeiner, D. P. 2011, *ApJ*, 737, 103  
 Schlegel D. J., Finkbeiner D. P., Davis M., 1998, *ApJ*, 500, 525  
 Rémy-Ruyer, A., Madden, S. C., Galliano, F. et al. 2015, *A&A*, 582, A121  
 Rowlands, K., Dunne, L., Maddox, S., et al. 2012, *MNRAS*, 419, 2545  
 Simard, L., Willmer, C. N. A., Vogt, N. P. et al. 2002, *ApJS*, 142, 1  
 Skibba, R. A., Engelbracht, C. W., Dale, D. . et al. 2011, *ApJ*, 738, 89  
 Sorce, J. G., Tully, R. B., Courtois, H. M. et al. 2014, *MNRAS*, 444, 527  
 Stickel, M., Lemke, D., Klaas, U., Krause, O., & Egner, S. 2004, *A&A*, 422, 39  
 Tuffs, R.J., Popescu, C.C., Pierini, D., et al. 2002, *ApJS*, 139, 37  
 Tully, R. B. & Fisher, J. R. 1977, *A&A*, 54, 661  
 Tully, R. B., Courtois, H. M., Dolphin, A. E. et al. 2013, *AJ*, 146, 86  
 Tuffs, R. J., Popescu, C. C., Völk, H. J., Kylafis, N. D., Dopita, M. A. 2004, *A&A*, 419, 821  
 Vlahakis, C., Dunne, L. & Eales, S. 2005, *MNRAS*, 364, 1253  
 Weingartner, J.C. & Draine, B.T. 2001, *ApJ*, 548, 296  
 Zibetti, S. & Groves, B. 2011, *MNRAS*, 417, 812

## APPENDIX A: PHOTOMETRY OF THE SAMPLE

We show here the figures analogous to Figs. 1&2, corresponding to the other 16 galaxies from our sample. Some considerations about the galaxies and the fits were added in the corresponding figure captions. While for some galaxies the fits to the observed surface brightness profiles are not perfect, one needs to take into account the particular features each galaxy image presented, which could not always be accurately modeled with a combination of an exponential and a Sérsic functions only.

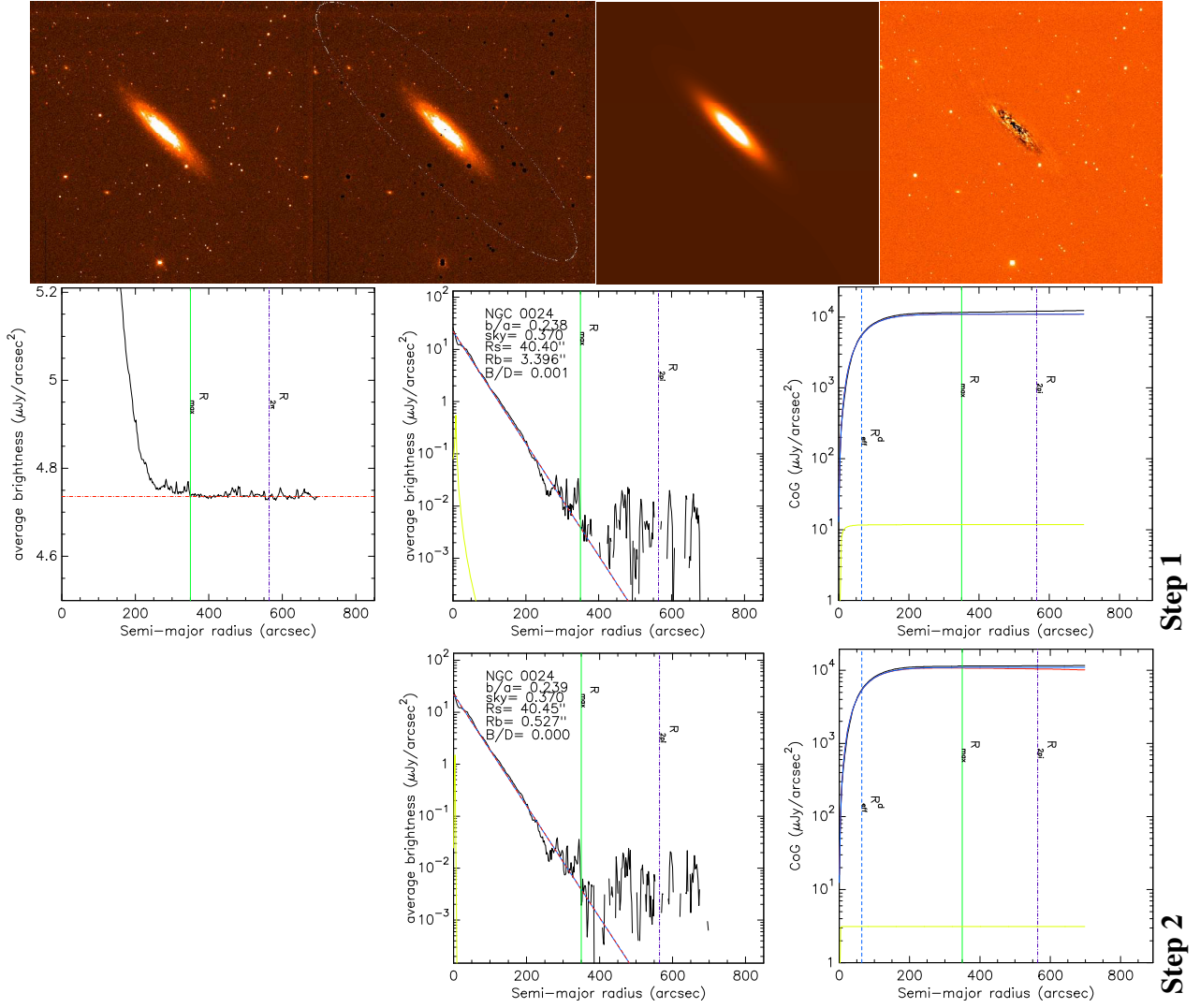


**Figure A1.** NGC0024 As for 1. The angular size of the observed image on the sky is  $14.82' \times 14.82'$ . This is basically a bulgeless galaxy. In the top row - 2nd panel from the left, the dashed white ellipse denotes  $R_{2\pi}$ , the major axis radius out to which data is available over the full azimuthal range. Step 3 fit was not necessary for this galaxy.

This paper has been typeset from a  $\text{\LaTeX}$  file prepared by the author.

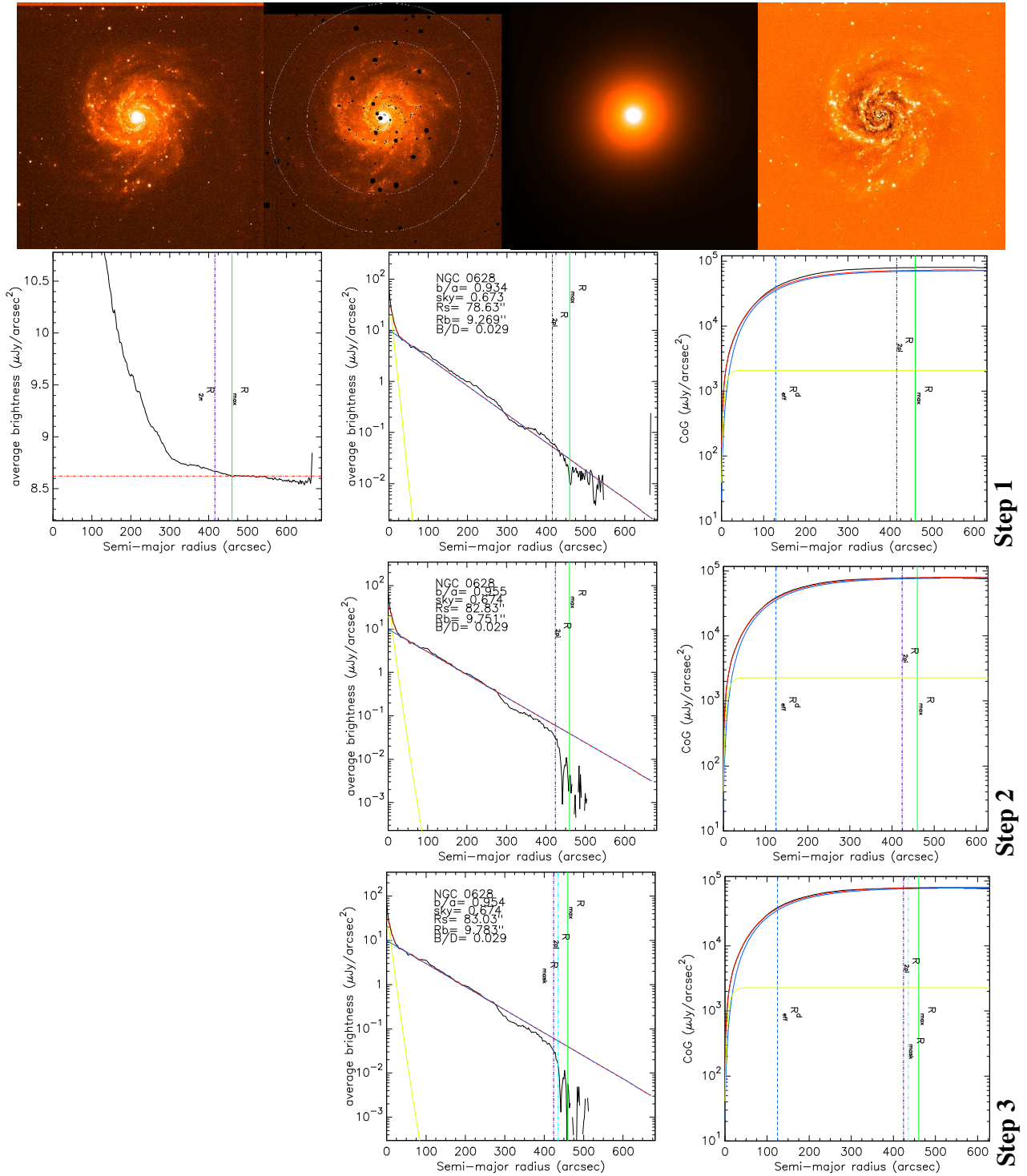
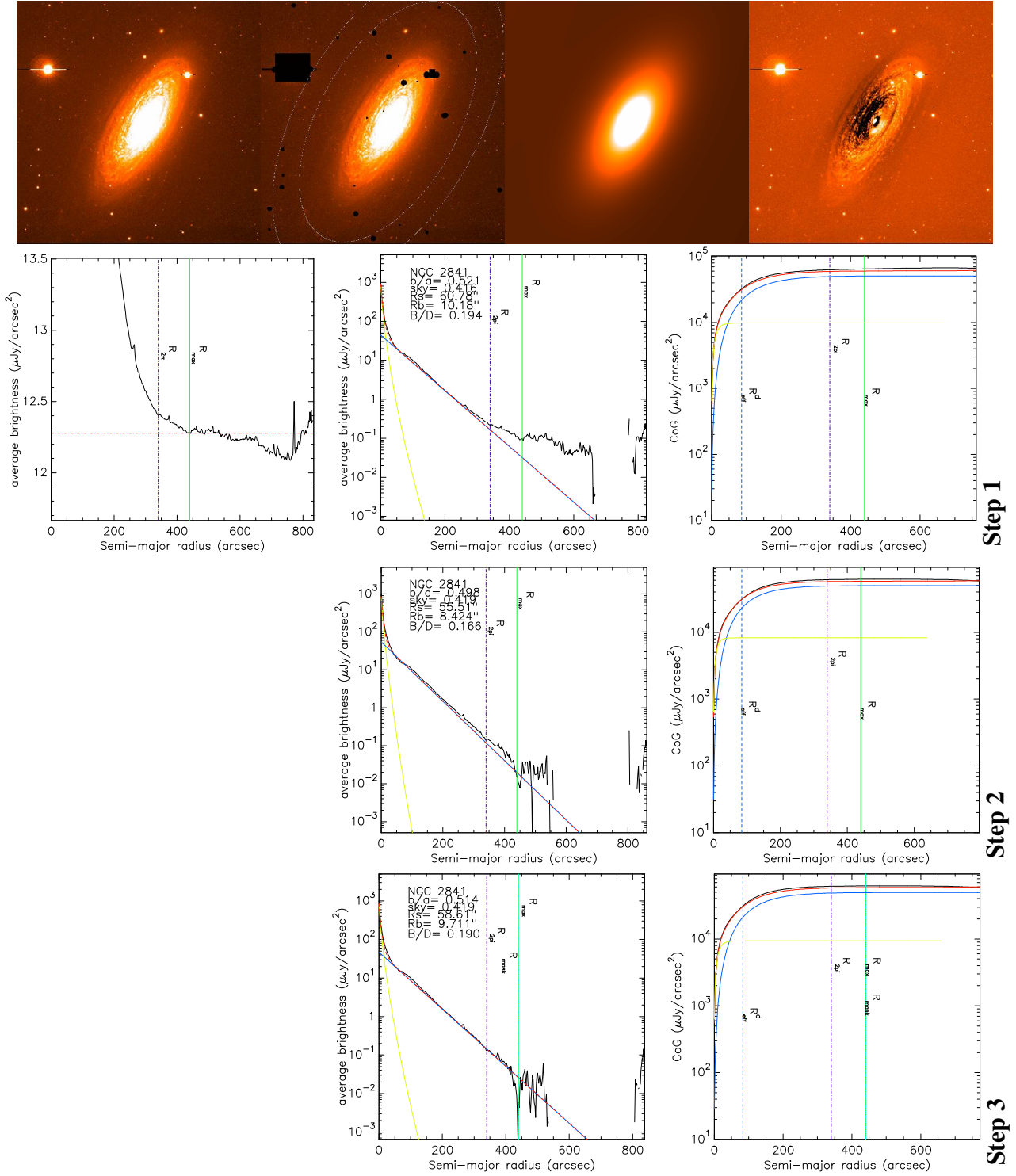
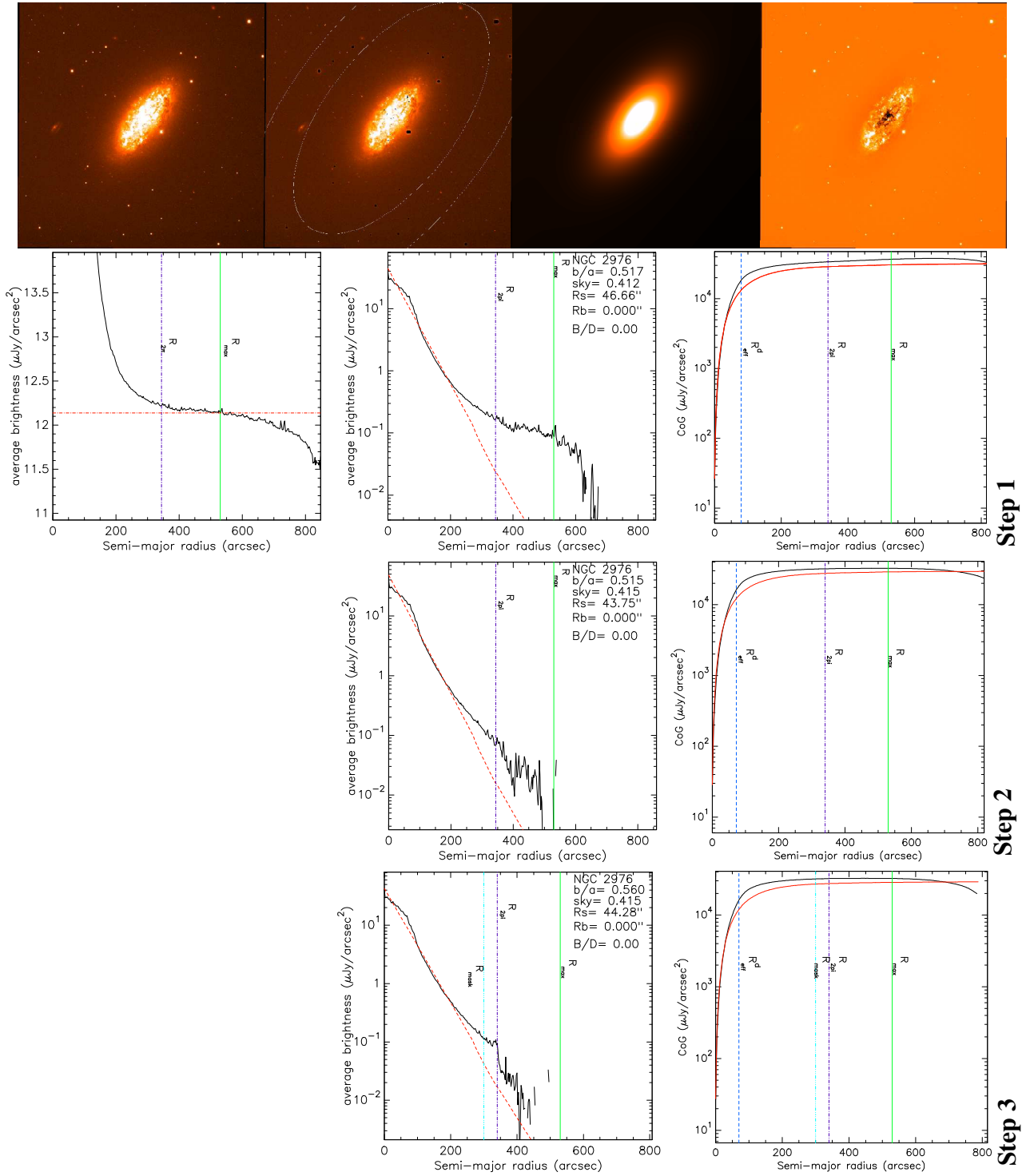


Figure A2. NGC0628 As for Fig. 2. The angular size of the observed image on the sky is  $14.82' \times 14.82'$ .



**Figure A3.** NGC2841 As for Fig. 2. In the top row - 2nd panel from the left, the two dashed white ellipses denote  $R_{2\pi}$  (inner ellipse, the major axis radius out to which data is available over the full azimuthal range and  $R_{max}$  (outer ellipse, the semi-major radius out to which emission from the galaxy could be detected). The observed image is potentially not large enough for a determination with greater precision of the background. The angular size of the observed image on the sky is  $10.38' \times 10.36'$ .



**Figure A4.** NGC2976 As for Fig. 2. This is essentially a bulgeless galaxy. Fitting with two components did not result a clear bulge. The angular size of the observed image on the sky is  $10.43' \times 10.45'$ .

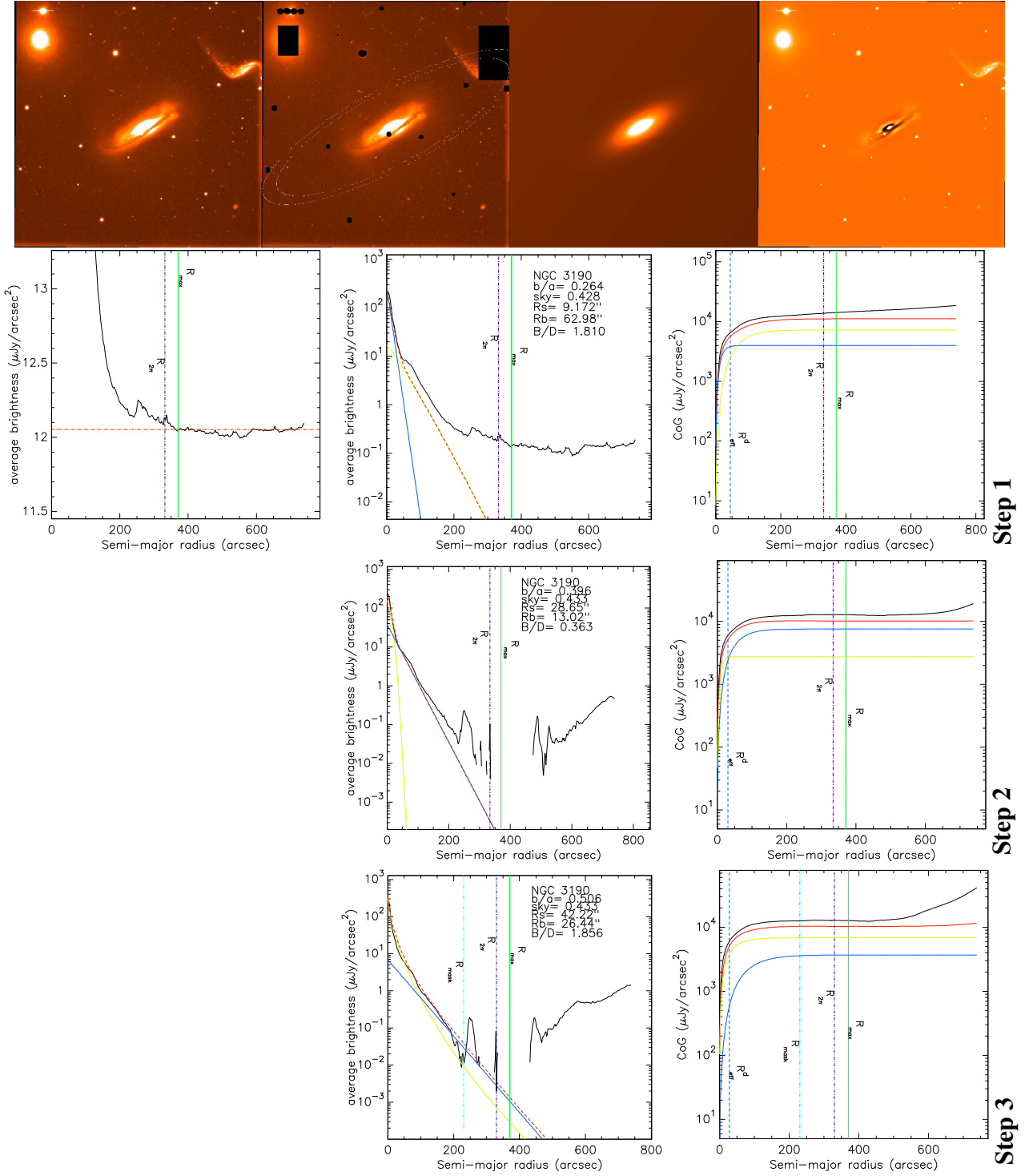


**Figure A5.** NGC3190 As for Fig. 2. This is a peculiar type of galaxy. The dust lane that surrounds the stellar disk creates difficulties in recovering an accurate surface brightness profile with a two-component fit. The angular size of the observed image on the sky is  $10.43' \times 10.43'$ .

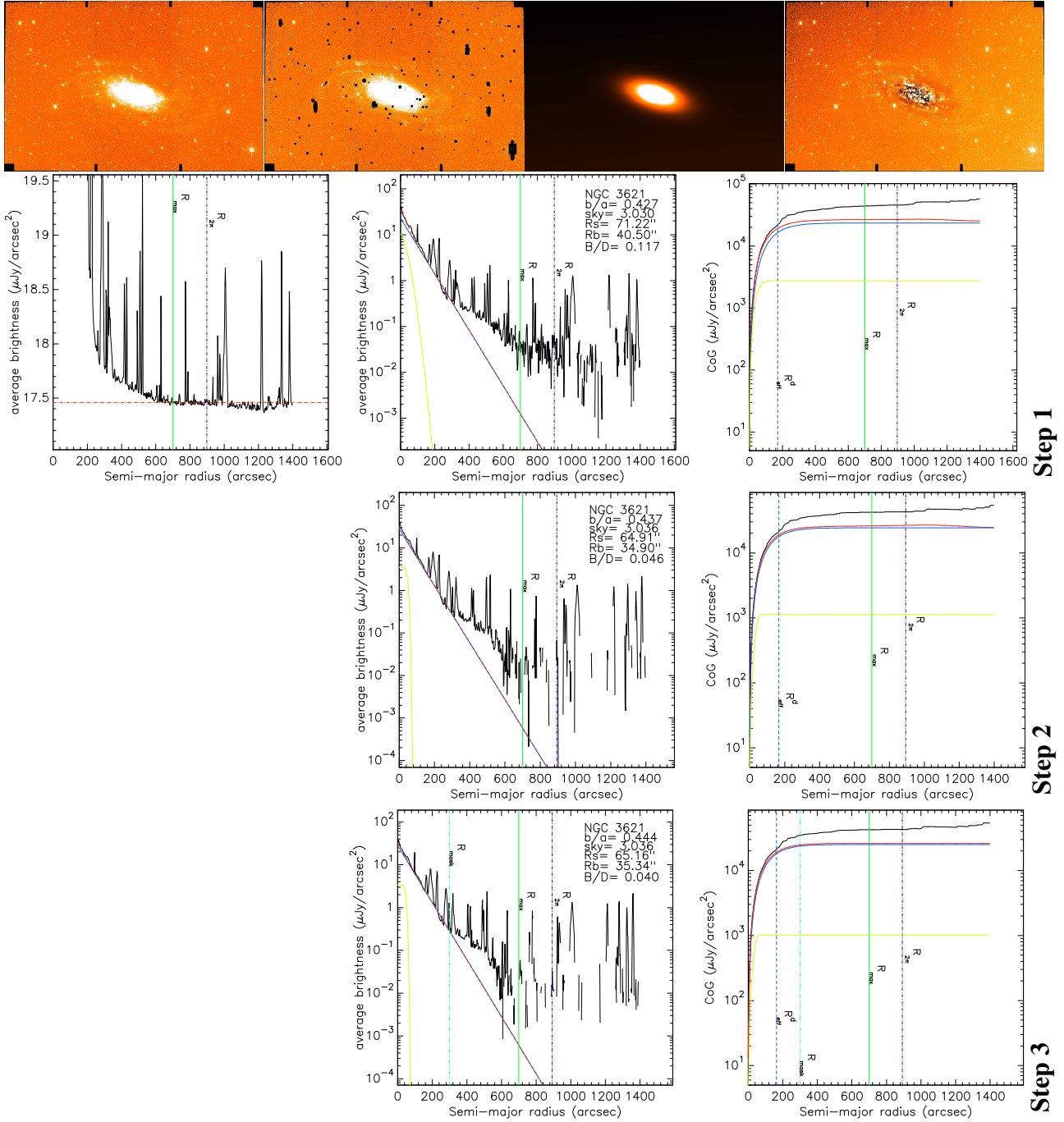


**Figure A6.** NGC3621 As for Fig. 2. The observed image for this galaxy was a large combined mosaic of multiple images, with a significant degree of noise. However, for the relevant galactocentric radii (up to 300 arcsecs., beyond which there is essentially noise and almost no galaxy emission), we managed to fit the surface brightness profile. The angular size of the observed image on the sky is  $29.08' \times 19.12'$ .

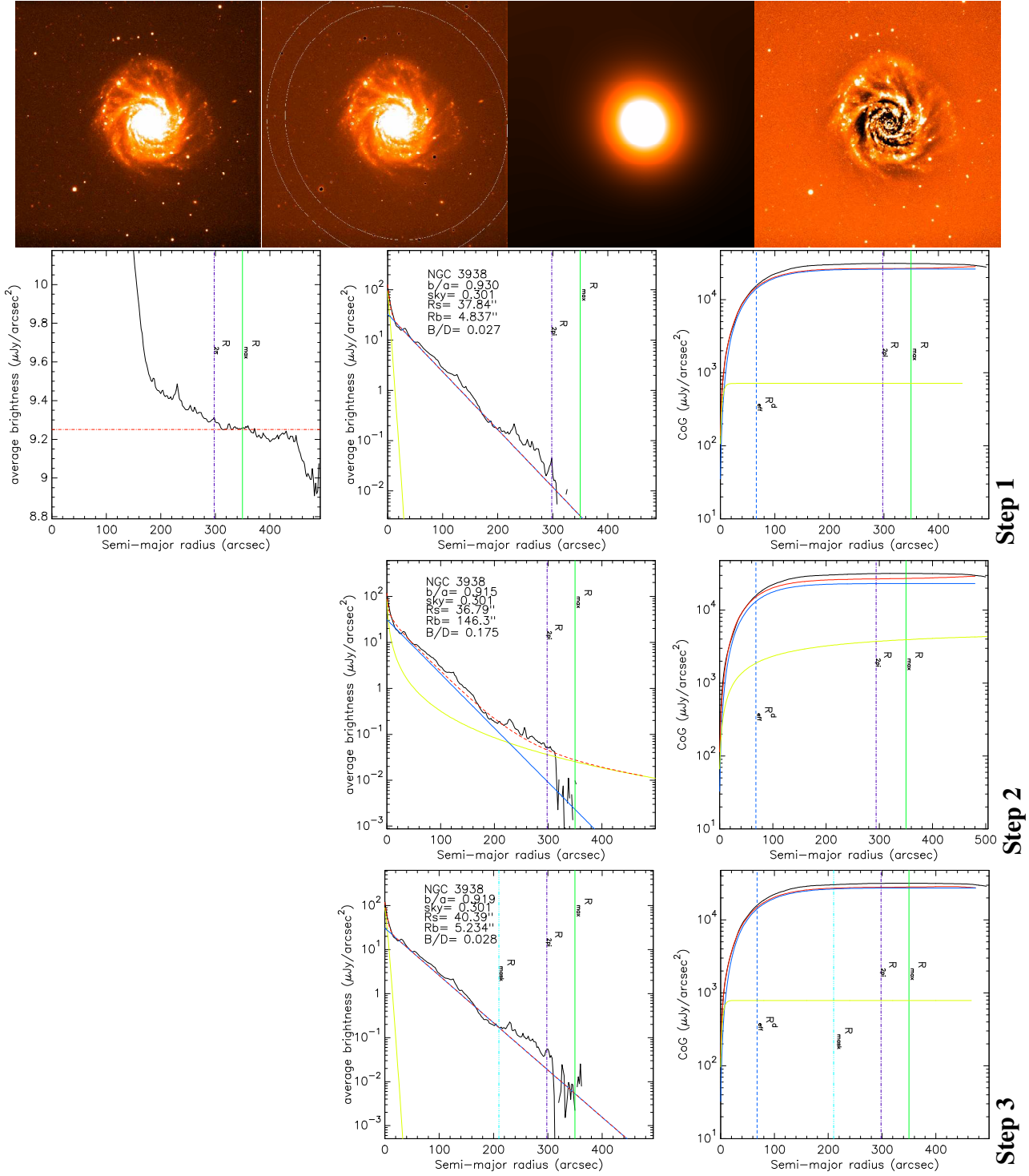


Figure A7. NGC3938 As for Fig. 2. The angular size of the observed image on the sky is  $9.88' \times 9.88'$ .

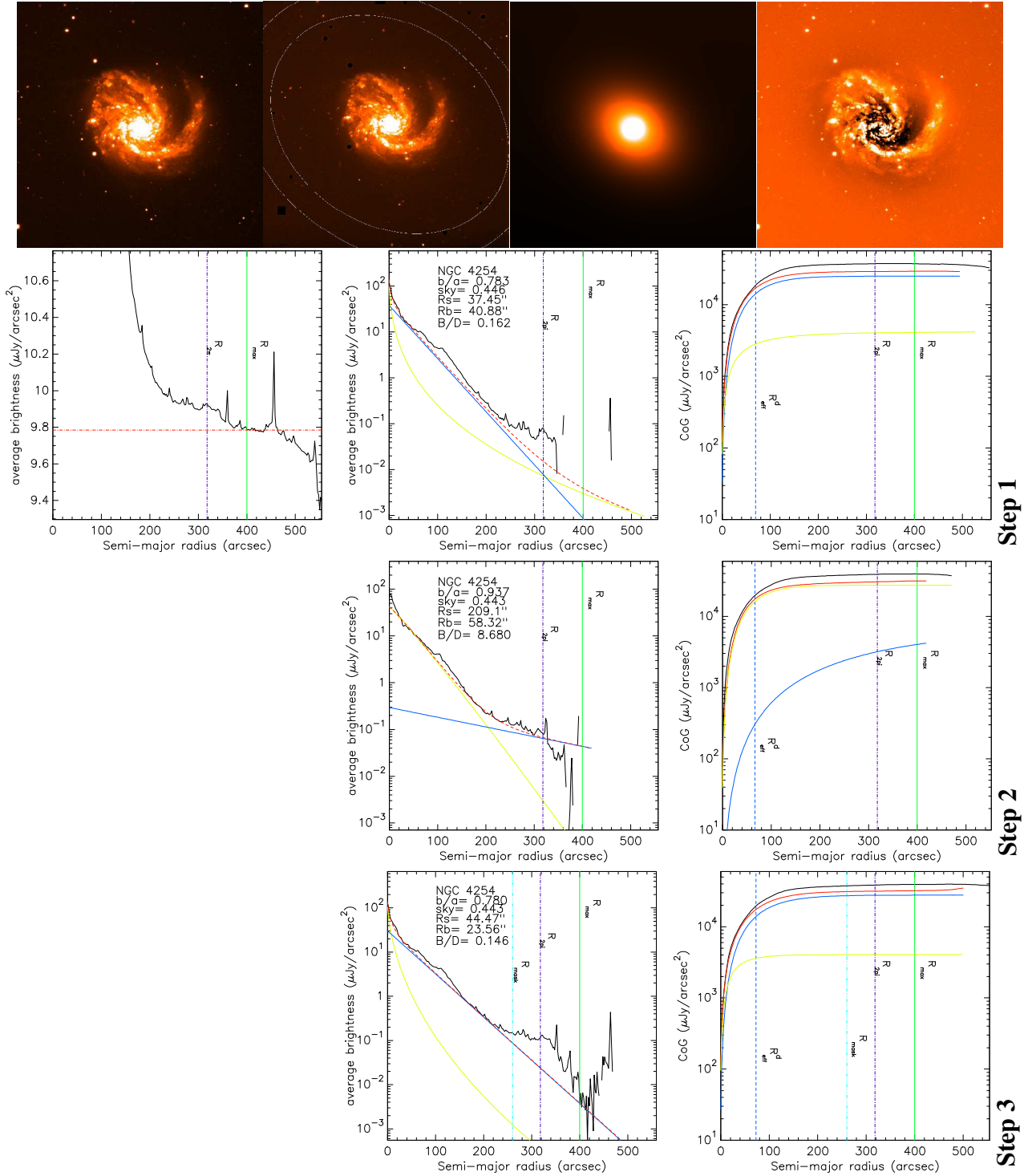
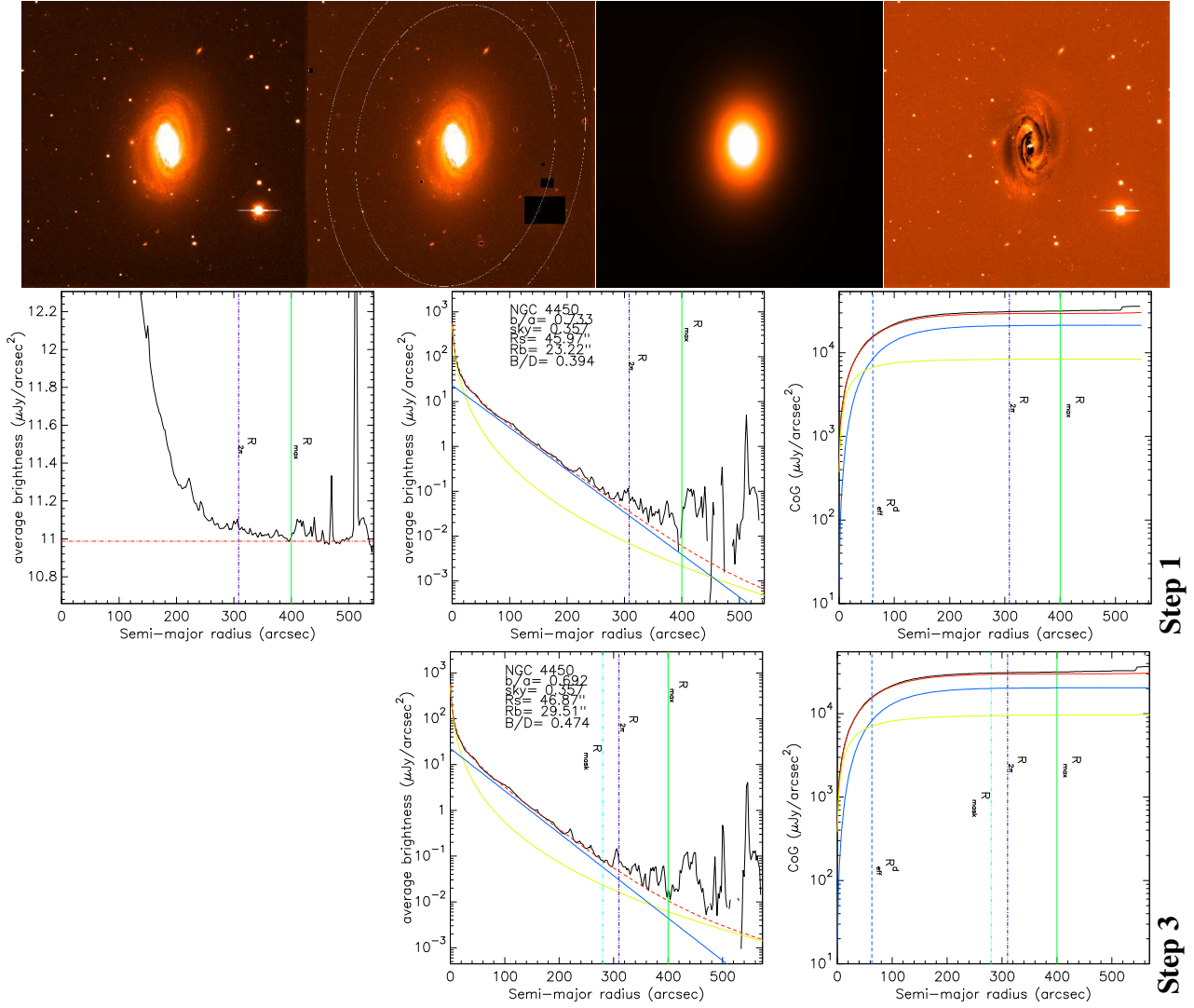
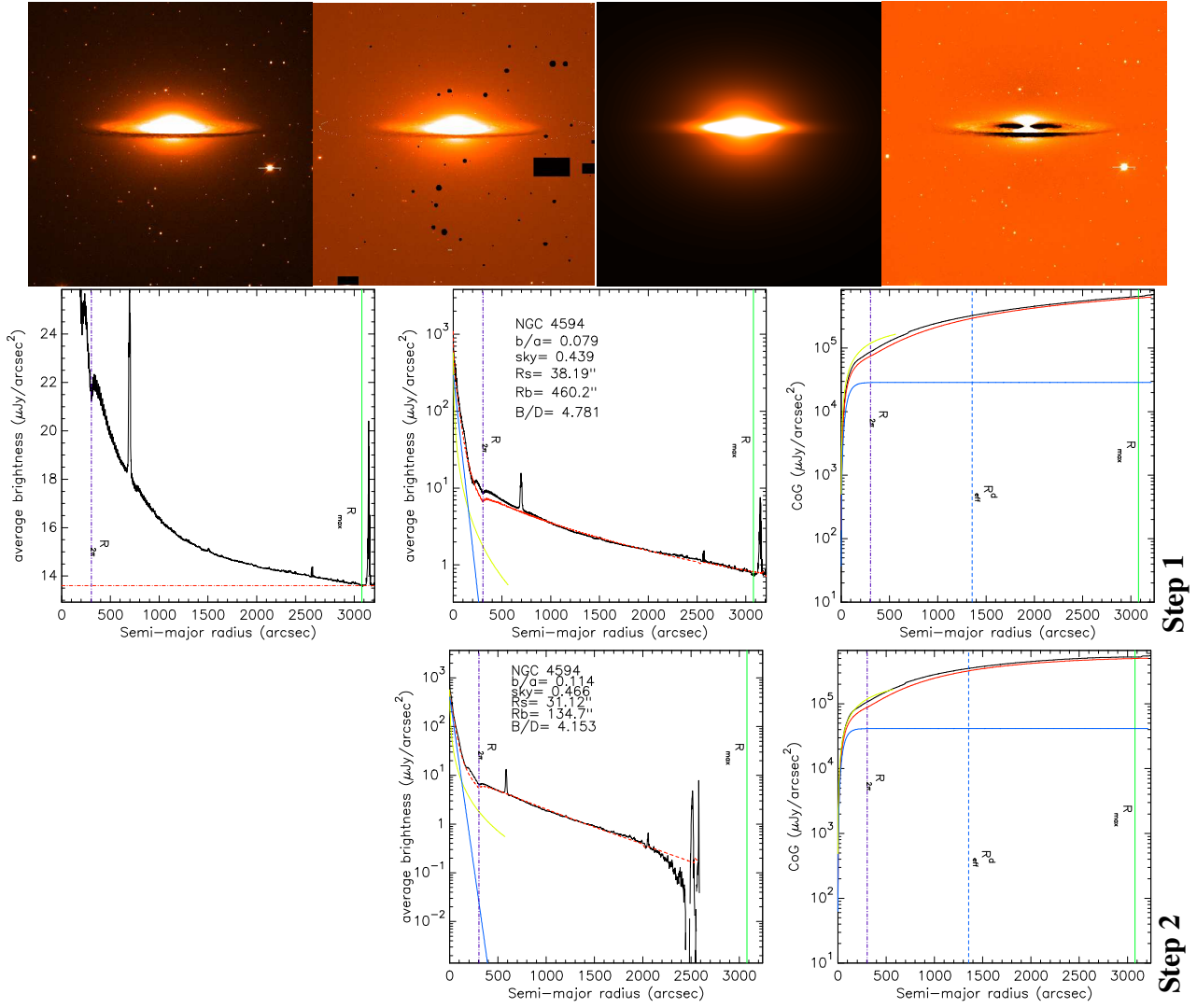


Figure A8. NGC4254 As for Fig. 2. The angular size of the observed image on the sky is  $10.36' \times 10.37'$ .



**Figure A9.** NGC4450 As for Fig. 2. Step 2 fits are not presented, as the fit was not meaningful. The angular size of the observed image on the sky is  $10.36' \times 10.36'$ .



**Figure A10.** NGC4594 As for Fig. 1. This is the so called “Sombrero Galaxy”, with a huge bulge, divided by the dust and stellar disks, and a large value for  $B/D$ . The fitting procedure was particularly complicated but we believe the results are meaningful. The angular size of the observed image on the sky is  $10.36' \times 10.37'$ .

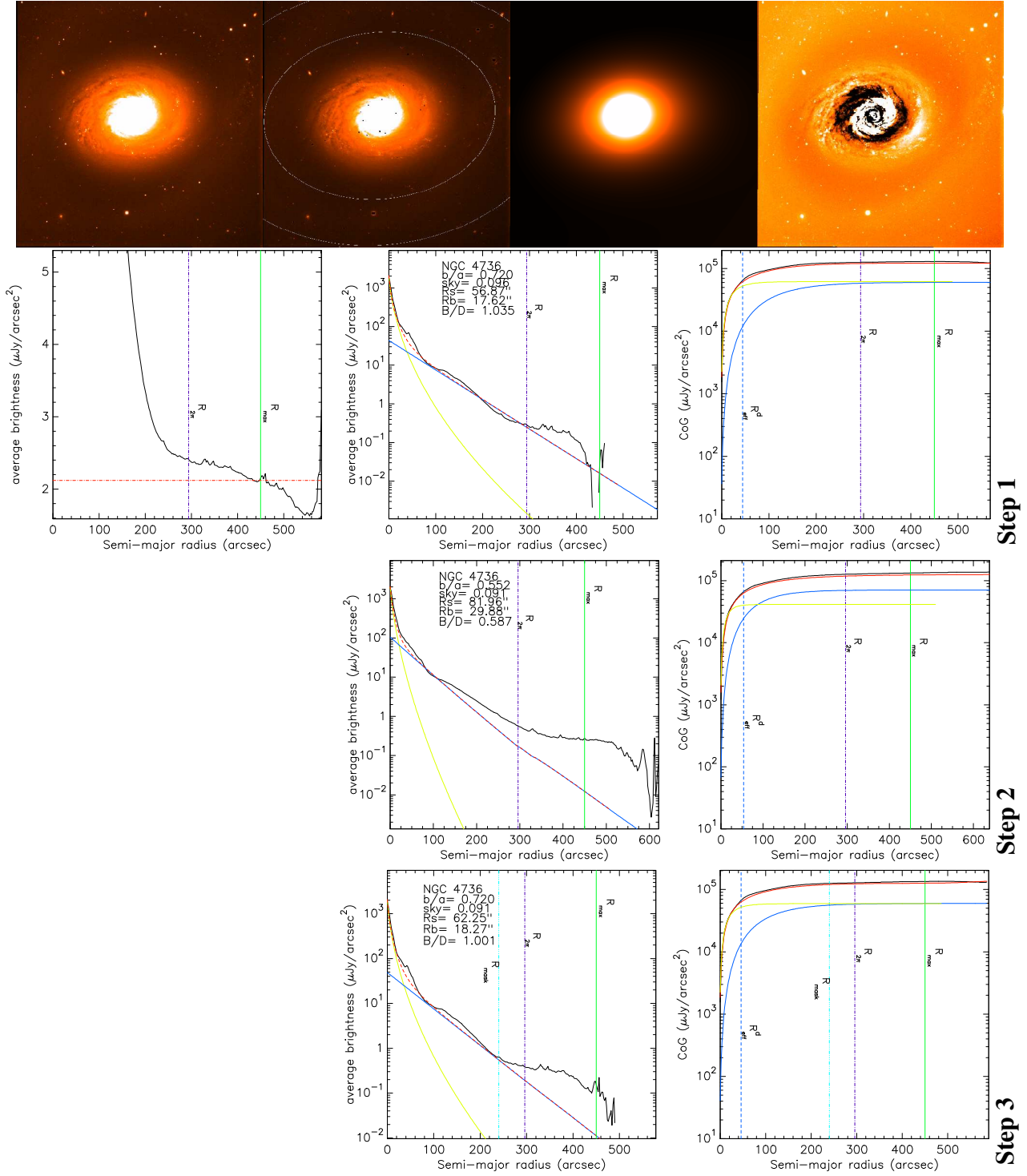
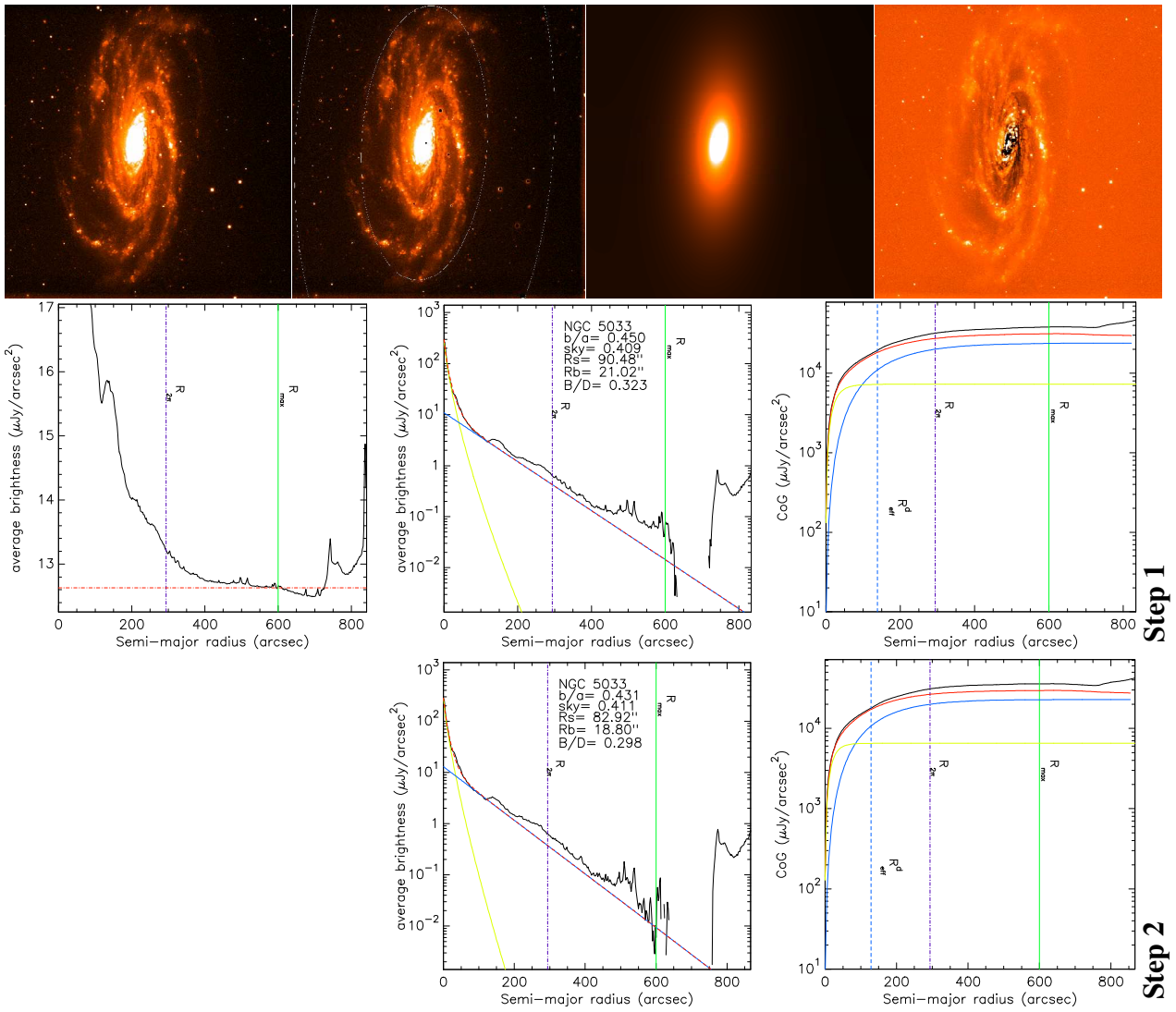


Figure A11. NGC4736 As for Fig. 2. The angular size of the observed image on the sky is  $10.41' \times 10.43'$ .



**Figure A12.** NGC5033 As for Fig. 1. The angular size of the observed image on the sky is  $10.36' \times 10.37'$ .

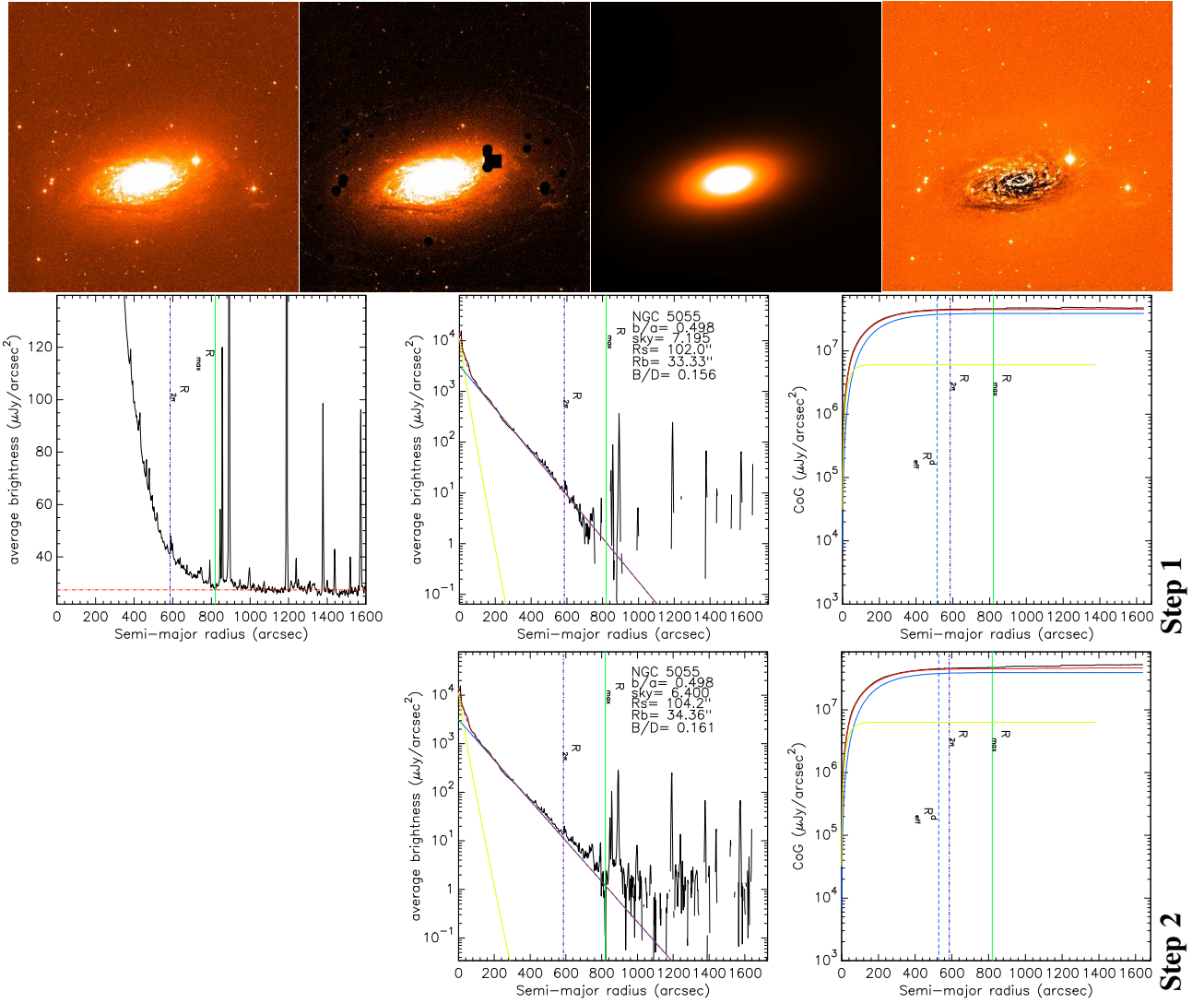
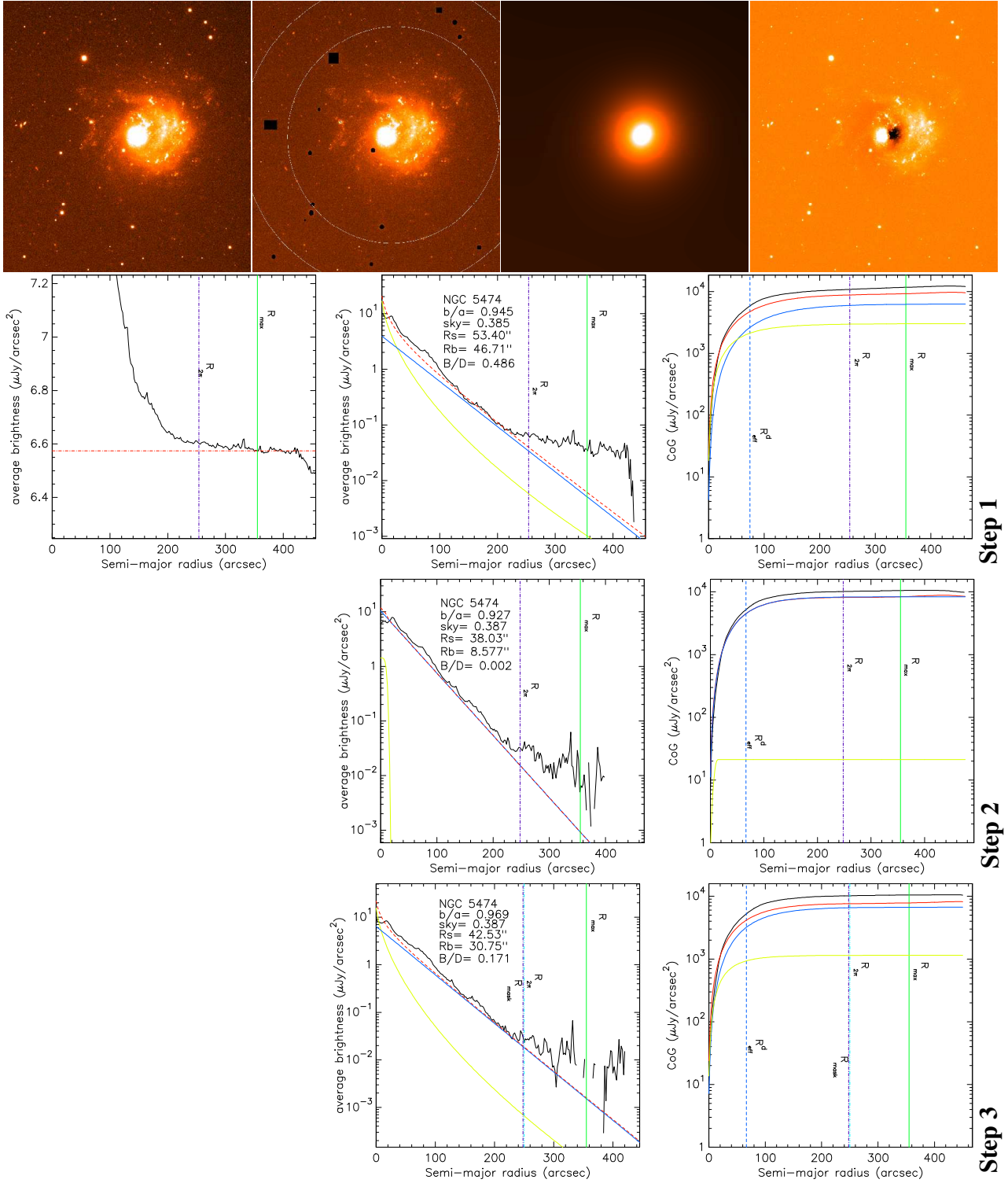


Figure A13. NGC5055 As for Fig. 1. The angular size of the observed image on the sky is  $20.30' \times 20.30'$ .



**Figure A14.** NGC5474 As for Fig. 2. This is an asymmetric galaxy, probably disturbed because of a merger. The fitting procedure was a bit more complex. The angular size of the observed image on the sky is  $18.50' \times 20.31'$ .

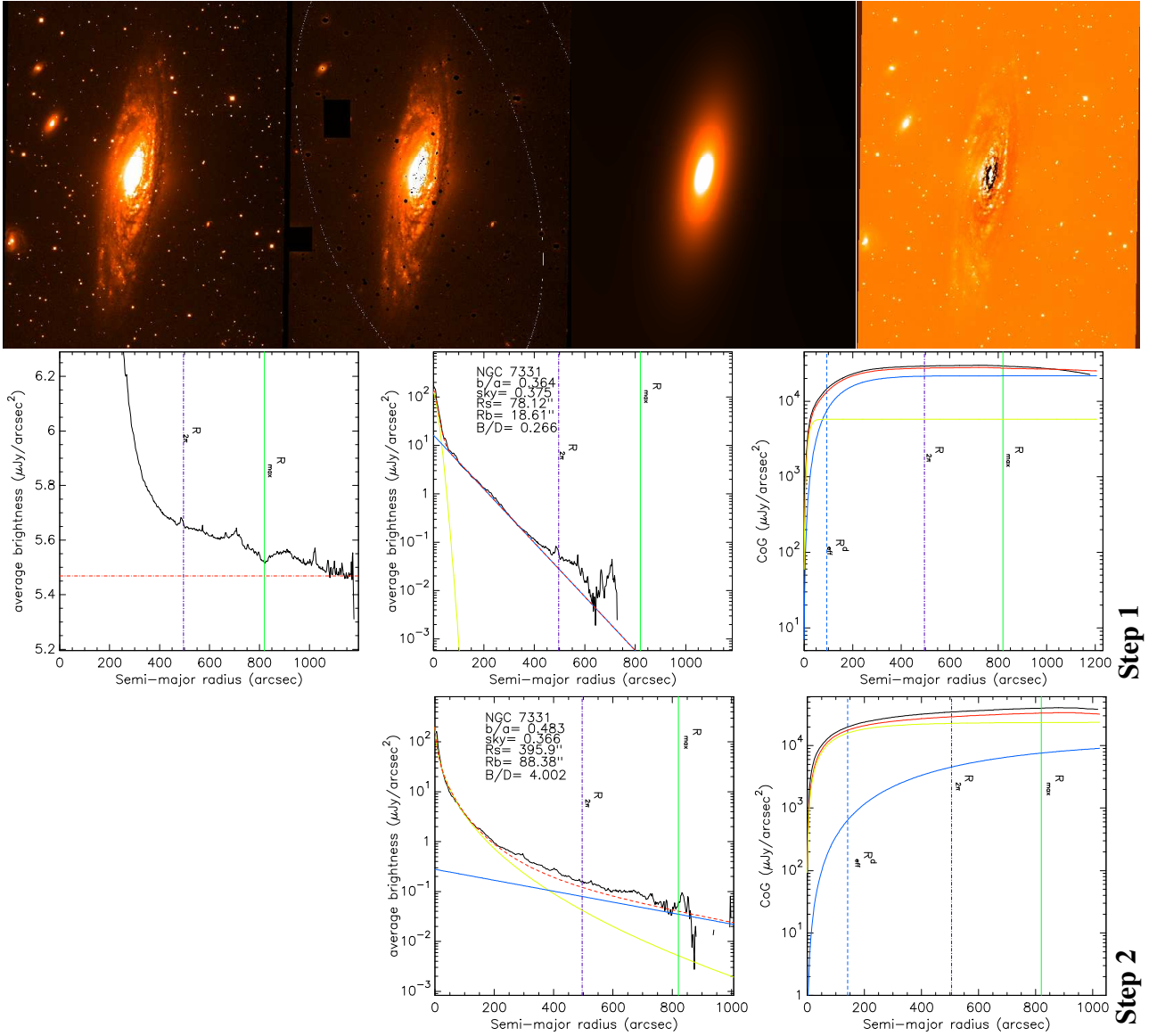


Figure A15. NGC7331 As for Fig. 1. The angular size of the observed image on the sky is  $10.59' \times 16.40'$ .

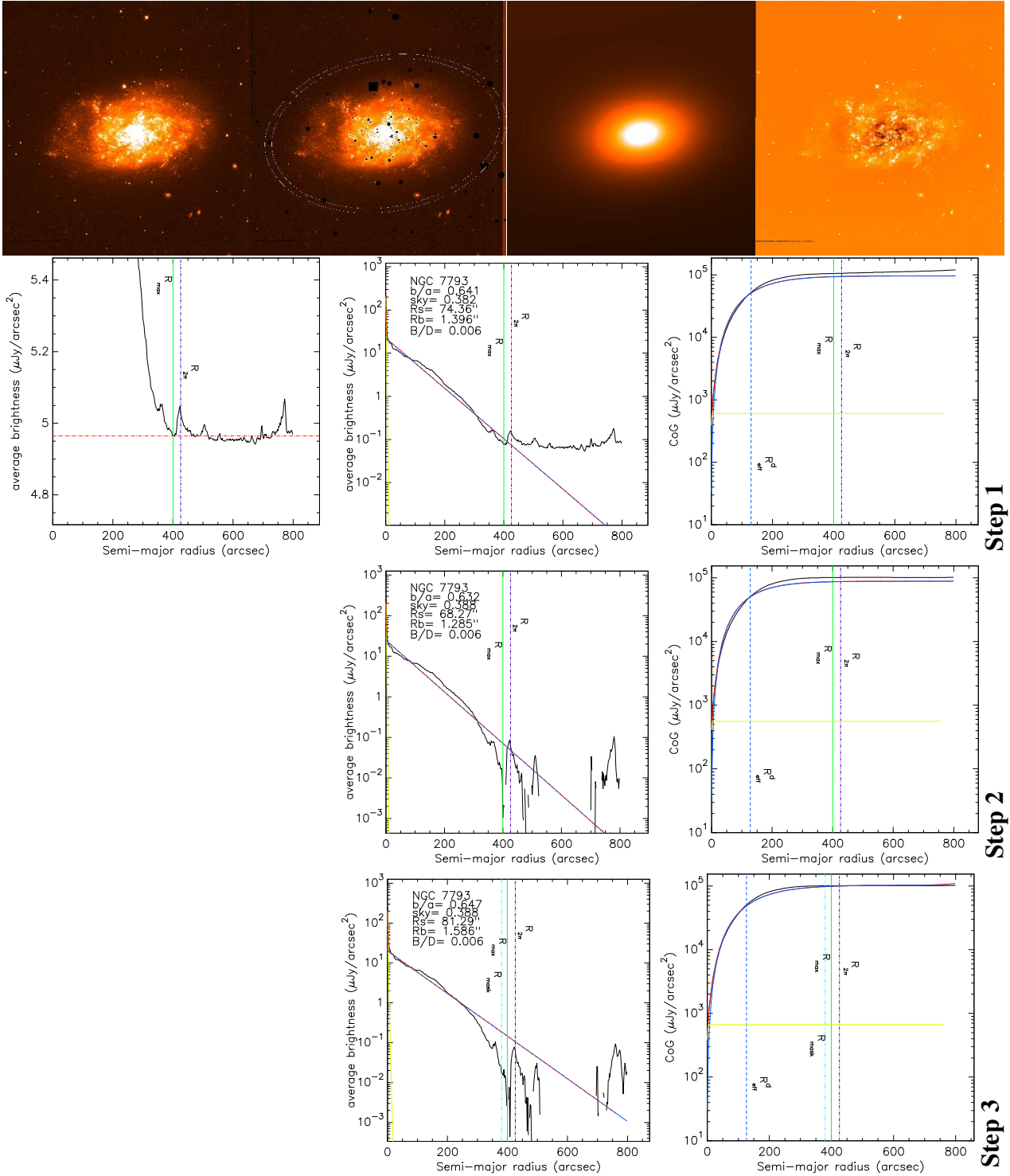


Figure A16. NGC7793 As for Fig. 2. The angular size of the observed image on the sky is  $14.83' \times 14.83'$ .